A STUDY IN BLUE: THE BARYON CONTENT OF ISOLATED LOW-MASS GALAXIES

JEREMY D. BRADFORD[1], MARLA C. GEHA[1], AND MICHAEL R. BLANTON[2]
[1] Astronomy Department, Yale University, New Haven, CT 06520, USA; jeremy.bradford@yale.edu, marla.geha@yale.edu
[2] Center for Cosmology and Particle Physics, New York University, New York, NY 10003, USA; blanton@nyu.edu

ABSTRACT

We study the baryon content of low-mass galaxies selected from the Sloan Digital Sky Survey (SDSS DR8), focusing on galaxies in isolated environments where the complicating physics of galaxy–galaxy interactions are minimized. We measure neutral hydrogen (HI) gas masses and line widths for 148 isolated galaxies with stellar mass between 10^7 and $10^{9.5} M_\odot$. We compare isolated low-mass galaxies to more massive galaxies and galaxies in denser environments by remeasuring HI emission lines from the Arecibo Legacy Fast ALFA survey 40% data release. All isolated low-mass galaxies either have large atomic gas fractions or large atomic gas fractions cannot be ruled out via their upper limits. We measure a median atomic gas fraction of $f_{\rm gas} = 0.81 \pm 0.13$ for our isolated low-mass sample with no systems below 0.30. At all stellar masses, the correlations between galaxy radius, baryonic mass, and velocity width are not significantly affected by environment. Finally, we estimate a median baryon to total dynamical mass fraction of $f_{\rm baryon,disk} = 0.15 \pm 0.17$. We also estimate two different median baryon to halo mass fractions using the results of semi-analytic models ($f_{\rm baryon,halo} = 0.04 \pm 0.06$) and abundance matching ($f_{\rm baryon,halo} = 0.04 \pm 0.02$). Baryon fractions estimated directly using HI observations appear independent of environment and maximum circular velocity, while baryon fractions estimated using abundance matching show a significant depletion of baryons at low maximum circular velocities.

Key words: galaxies: dwarf – galaxies: evolution – galaxies: ISM – galaxies: kinematics and dynamics

Supporting material: machine-readable table

1. INTRODUCTION

Environment plays a major in role in the evolution and the observed properties of galaxies (e.g., Dressler 1980; Kauffmann et al. 2004; Blanton et al. 2005a; Peng et al. 2010; Geha et al. 2012; Tal et al. 2014; Wetzel et al. 2014). Environmental processes such as tidal forces and ram-pressure stripping shape, quench, and destroy galaxies (e.g., Gunn & Gott 1972; Toomre & Toomre 1972; Moore et al. 1996; Peñarrubia et al. 2008). These processes will be especially pronounced in low-mass galaxies with stellar masses below $10^9 M_\odot$, where more massive nearby galaxies dramatically affect the local gravitational potential (e.g., Kravtsov et al. 2004; Zolotov et al. 2012; Kenney et al. 2013).

The effects of environment complicate both observational interpretations and comparisons to theoretical predictions of galaxy formation. Galaxies in isolation are *relatively* undisturbed by environmental processes. Thus, isolated galaxies can potentially present a clearer picture of galaxy evolution (Karachentseva 1973; Barton et al. 2007; Cortese et al. 2011; Karachentsev et al. 2011; Tollerud et al. 2011; Toribio et al. 2011). Recent work has found that the properties of isolated low-mass galaxies, loosely defined as "field galaxies," appear to conflict with small-scale predictions of ΛCDM cosmology (Kirby et al. 2014; Klypin et al. 2014; Papastergis et al. 2015). It is critical that isolated low-mass galaxies are clearly defined and well studied.

Isolated galaxies retain their HI gas out to larger radii (e.g., Begum et al. 2008), contain a large fraction of baryons in atomic gas (e.g., Geha et al. 2006, hereafter G06; Grcevich & Putman 2009), and are predicted to exhibit larger maximum circular velocities than galaxies that have been tidally stripped (e.g., Brooks & Zolotov 2014). Therefore, in underdense regions, where galaxies are less affected by environmental

processes, it might be easier to predict their properties when compared to galaxies in dense environments (McGaugh & Wolf 2010; Cortese et al. 2011; Huang et al. 2012a; Argudo-Fernández et al. 2014).

Here we present the largest homogeneously measured data set of baryons in isolated low-mass galaxies with $10^7 M_\odot < M_* < 10^{9.5} M_\odot$. Our new data probe isolated galaxies with average circular velocities of $45\,\mathrm{km\,s^{-1}}$ and average baryon masses of $2 \times 10^8\, M_\odot$, with circular velocities as low as $\sim 20\,\mathrm{km\,s^{-1}}$ and baryon masses as low as $\sim 10^{7.4} M_\odot$. We complement the existing Arecibo Legacy Fast ALFA (ALFALFA) 40% data release of Haynes et al. (2011, hereafter ALFALFA40), with new 21 cm observations, incorporating our isolation criterion into the selection of 148 low-mass targets.

This paper is organized as follows: in Section 2, we introduce the data, define our isolation criteria, and describe our automated HI parameter estimates. In Section 3, we present our results, examining the relationship between galaxy stellar mass, atomic gas mass, and atomic gas fraction (Sections 3.1 and 3.2), the relationship between galaxy size, baryonic mass and dynamical mass (Section 3.3), and finally baryon fractions in Section 3.4. In Section 4, we discuss our results in context with the literature, particularly with respect to the effects of environment on galaxy properties. Finally, we summarize our findings in Section 5.

Throughout this work we assume the following cosmological parameters: $\Omega_0 = 0.3$, $\Omega_\Lambda = 0.7$, $H_0 = 70\,\mathrm{km\,s^{-1}}$ (i.e., $h = 0.7$), and a cosmic baryon fraction of $f_{\rm b} = 0.17$ (Komatsu et al. 2011). We present a small sample of isolated low-mass galaxies for reference in Table 1. Since our HI observations are ongoing, our complete data set and raw HI spectra are available upon request. This paper is the first in a series using isolated low-mass galaxies as a control sample for testing galaxy evolution at small scales.

Table 1
Isolated Galaxy Data Sample

NSA ID	α (J2000.0) (h : m : s)	δ (J2000.0) (° : ′ : ″)	Distance (Mpc)	Inclination (deg)	$V_{W20,i}$ (km s^{-1})	$r_{\rm eff}$ (kpc)	$M_{\rm HI}$ ($10^9 M_\odot$)	M_* ($10^9 M_\odot$)	Source
(1)	(2)	(3)	(4)	(5)	(6)	(7)	(8)	(9)	(10)
162	09:58:30.23	+00:02:42.72	30.23 ± 1.89	71	40 ± 3	0.72 ± 0.04	0.105 ± 0.029	0.016 ± 0.007	1
1443	12:23:09.98	+00:25:37.76	35.36 ± 2.00	68	26 ± 13	0.86 ± 0.05	0.041 ± 0.019	0.043 ± 0.020	1
5109	22:30:36.80	−00:06:37.01	21.26 ± 1.86	28	78 ± 3	0.29 ± 0.02	0.067 ± 0.024	0.008 ± 0.004	3
5378	23:06:39.16	+00:34:41.02	68.13 ± 2.39	70	62 ± 2	1.82 ± 0.06	1.039 ± 0.166	0.273 ± 0.126	1
5424	23:14:19.43	+00:10:59.36	60.30 ± 1.75	88	64 ± 3	1.77 ± 0.05	0.405 ± 0.058	0.612 ± 0.282	1
5449	23:28:12.31	−01:03:46.37	35.30 ± 2.14	60	49 ± 2	1.08 ± 0.07	0.229 ± 0.059	0.020 ± 0.009	3
5720	00:13:44.02	+00:22:18.46	56.50 ± 1.75	60	24 ± 1	0.85 ± 0.03	0.337 ± 0.049	0.097 ± 0.045	1
6186	00:57:56.60	+00:52:08.56	30.17 ± 2.86	62	47 ± 2	0.69 ± 0.07	0.150 ± 0.059	0.051 ± 0.024	3
6368	01:09:07.85	+01:07:15.89	15.97 ± 1.64	55	39 ± 1	0.60 ± 0.06	0.061 ± 0.026	0.015 ± 0.007	1
6412	01:13:45.98	+00:56:44.13	104.68 ± 2.14	75	78 ± 11	1.57 ± 0.03	0.766 ± 0.135	0.788 ± 0.363	1
6748	01:26:05.01	+00:19:00.68	24.85 ± 2.00	71	72 ± 1	1.39 ± 0.11	0.461 ± 0.152	0.088 ± 0.040	3
6949	01:55:59.76	−00:11:08.02	51.69 ± 1.75	60	60 ± 5	0.95 ± 0.03	0.208 ± 0.039	0.323 ± 0.149	1
7167	02:18:08.02	+00:45:29.39	39.84 ± 2.32	56	77 ± 1	1.16 ± 0.07	0.371 ± 0.091	0.139 ± 0.064	1
8260	00:35:06.49	+14:21:17.42	170.84 ± 2.14	63	161 ± 26	5.61 ± 0.07	14.956 ± 3.551	25.029 ± 11.528	2
8266	00:32:00.11	+14:44:17.36	142.07 ± 2.14	67	139 ± 3	7.84 ± 0.12	11.555 ± 1.152	7.108 ± 3.274	2

Note. Properties of 15 isolated NSA galaxies that have been observed in HI. Columns are (1) the NASA Sloan Atlas v0.1.2 (NSA) identifier for all galaxies, which is unique to this iteration of the NSA catalog, (2) R.A., (3) decl., (4) heliocentric luminosity distance, (5) inclination angle, (6) inclination-corrected velocity width of the 21 cm line at 20% peak flux, (7) effective radius, (8) HI mass, (9) stellar mass and (10) primary source of HI observation with 1: our study, 2: the Haynes et al. (2011) ALFALFA survey and 3: Geha et al. (2006).

(This table is available in its entirety in machine-readable form.)

2. DATA

2.1. Galaxy Catalog

To construct a sample of isolated low-mass galaxies, we begin with the NASA Sloan Atlas[3] (NSA) catalog (Blanton et al. 2011), which is itself a re-reduction of the SDSS Data Release 8 (DR8; Aihara et al. 2011). This sample was first described in (Geha et al. 2012, hereafter G12), and we provide a brief description here.

The NSA re-reduction is optimized for nearby extended objects with $z < 0.055$ (Blanton et al. 2011). The NSA photometry includes image mosaics from both SDSS *ugriz* and *GALEX* FUV, NUV bands (Martin et al. 2005). Sérsic model structural parameters are fit using the SDSS *r*-band image. The SDSS spectra are also reanalyzed and recalibrated (Yan 2011; Yan & Blanton 2012). The spectra equivalent widths are re-measured and included in the NSA catalog.

In order to ensure accurate distance estimates and to stay within the spectroscopic completeness limits of the SDSS, we discard any galaxy in the NSA catalog where it is not detected in the SDSS *g*, *r*, or *i* passbands and only include galaxies with spectroscopy from the main SDSS legacy survey with $z > 0.002$ and $M_r < 17.72$. We also discard galaxies where the Sérsic half-light radius is larger than the Petrosian 90% light radius, which indicates that surface brightness model fitting has failed. Our final catalog is comprised of 106,374 galaxies that span distances of $10 < D < 250$ Mpc and stellar masses of $10^{6.1} M_\odot < M_* < 10^{11.9} M_\odot$.

Galaxy stellar masses (M_*) are calculated in the NSA catalog using the kcorrect software of Blanton & Roweis (2007) using the SDSS and *GALEX* photometric bands and assuming a Chabrier (2003) IMF. The error in stellar mass is estimated from the scatter between models examined by Blanton &

Roweis (2007), who found roughly uniform differences of 0.2 dex between models (see their Figure 17). We calculate luminosity distances using SDSS redshifts corrected for peculiar velocities using the model of Willick et al. (1997), who compiled a velocity–distance catalog of spiral galaxies using Tully–Fisher calibrated distances and redshift velocities. Distance uncertainties are folded into all distance-dependent calculations.

2.2. Galaxy Environments, Isolation Criteria, and Sample Definition

Many methods have been devised for quantifying the local and large-scale environments around galaxies. To measure environment density and degree of isolation, it is common to define an environment variable, such as the nth nearest neighbor surface density (e.g., Brough et al. 2013) or tidal force index (e.g., Karachentsev et al. 2011). It is also common to define galaxies "in the field" in order to study galaxies in isolation, where such a galaxy has various definitions in the literature. Other studies measure the density of galaxies within a fixed-aperture on the sky or measure two-dimensional (2D) projected distances between galaxies with cuts applied in redshift space (e.g., Croton et al. 2005; Conroy et al. 2007; Gallazzi et al. 2008, G12). See Muldrew et al. (2011) for a comparison of 20 different environment definitions applied to a mock galaxy catalog.

Our goal is not to review and test the various methods of quantifying environment. Our goal is to select the most isolated galaxies where environmental processes are minimized. G12 has found that low-mass galaxies with $10^7 M_\odot < M_* \leqslant 10^9 M_\odot$ are always star-forming when located more than 1.5 Mpc from a massive host. In our work, we assume that environment has not significantly affected such low-mass galaxies and we adopt the results of G12 as our isolation criterion for low-mass galaxies (also see Wheeler et al. 2014).

---

[3] http://www.nsatlas.org

For low-mass galaxies with $M_* \leqslant 10^{9.5} M_\odot$, we calculate the 2D projected distance (d_{host}) to the nearest more massive host within a redshift of $1000 \, \mathrm{km \, s^{-1}}$ and within a 2D projected distance of 7 Mpc. Massive neighbors may be located beyond the edges of the SDSS survey; therefore, we also search for massive hosts beyond the SDSS footprint using the 2MASS Extended Source Catalog (Jarrett et al. 2000). A galaxy is considered massive if $M_* \gtrsim 2.5 \times 10^{10} M_\odot$ (the 2MASS magnitude $M_{K_s} < -23$). Therefore, massive hosts are at least ~ 0.5 dex more massive than the low-mass galaxies. Redshifts for 2MASS hosts are obtained using a variety of other surveys and literature as described in G12. We therefore define a low-mass galaxy to be isolated if $d_{host} > 1.5$ Mpc. We set $d_{host} = 7$ Mpc if no such nearby massive host is found.

Since the results of G12 apply only to low-mass galaxies, the above isolation criterion is ill-defined for massive galaxies. To select a small sample of isolated massive galaxies in the NSA catalog with $M_* > 10^{9.5} M_\odot$, G12 created a modified Tinker et al. (2011) group catalog where the central galaxies in the group catalog were defined to be located at least three times their halo radius from another central galaxy. We define our high-mass isolated criteria by successfully recovering these isolated massive galaxies from the modified Tinker et al. (2011) group catalog.

For high-mass galaxies with $M_* > 10^{9.5} M_\odot$, we similarly measure the 2D projected separation to the nearest more massive galaxy by at least 0.5 dex in stellar mass within a 2D projected distance of 7 Mpc and within $1000 \, \mathrm{km \, s^{-1}}$ in redshift. We call this distance $d_{host,0.5}$. We place the same cut on $d_{host,0.5}$ of 1.5 Mpc as the low-mass sample.

The cut on $d_{host,0.5}$ is not applicable to the most massive galaxies in our sample because too few or no massive galaxies exist above 0.5 dex in mass. Therefore, we use the SDSS and 2MASS catalogs to measure the fifth nearest neighbor surface density ($\Sigma_n = n/\pi r_n^2$), where n is smaller if less than five neighbors are found within 7 Mpc. To be isolated, we require $\Sigma_n < 1 \, \mathrm{Mpc^{-2}}$. This cut on Σ_n is motivated by the modified Tinker et al. (2011) group catalog, since we maximize the recovery of this catalog by cutting on $\Sigma_n < 1 \, \mathrm{Mpc^{-2}}$. Decreasing the cutoff in Σ_n does not appreciably effect our results. Removing this cut entirely will affect our results by including one gas-depleted galaxy at high masses relative to the rest of the sample (see Section 3.2). Therefore, to be considered isolated, we require a massive galaxy to have both $d_{host,0.5} > 1.5$ Mpc and $\Sigma_n < 1 \, \mathrm{Mpc^{-2}}$.

Our isolated low-mass galaxies may have a nearby neighbor with similar stellar mass that has not been captured by d_{host} (e.g., Stierwalt et al. 2015). We calculate the 2D projected separation to the nearest more massive galaxy (d_{pair}) for all galaxies with $M_* < 10^{10} M_\odot$. We use this environment variable to avoid radio beam confusion. We only require that $d_{pair} > 2r_{beam}$, where the beam radius (r_{beam}) is defined in Equation (10) below. Both halves of the overlapping pair are removed. We discard 53 galaxies, both isolated and non-isolated, with overlapping beams, all of which are from the ALFALFA survey. We find no motivation to place further restrictions on d_{pair}. In summary:

    a. A low-mass galaxy is isolated if $M_* < 10^{9.5} M_\odot$ and $d_{host} > 1.5$ Mpc.

    b. A high-mass galaxy is isolated if $M_* > 10^{9.5} M_\odot$, $d_{host,0.5} > 1.5$ Mpc and $\Sigma_n < 1 \, \mathrm{Mpc^{-2}}$.

Table 2
HI Observation Details

Run ID	Avg. Integration Time (s)	N Reduced	N High Quality	N Non-detections	N Bad Baselines
GBT2008	802	184	141	43	12
AO2005	796	32	32	0	3
AO2013	459	83	80	3	8
AO2014a	499	51	47	4	0
AO2014b	571	21	17	4	0

Note. Observing run identifier, average integration time, number of reduced spectra, number of high-quality spectra, number of non-detections, number of bad baselines for all of our HI observations. Note that GBT has a smaller dish diameter than Arecibo; therefore, integration times are not directly comparable.

We refer to all galaxies that do not meet our isolation criteria as "non-isolated" for the duration of this paper.

In terms of central and satellite galaxies: all isolated galaxies are central galaxies. All satellite galaxies are categorized as non-isolated. Due to the strictness of our isolation criteria, many non-isolated galaxies would be categorized as central galaxies. We define 36,592 galaxies as isolated and 69,782 galaxies as non-isolated in our catalog of 106,374 total galaxies. We generally assume that our isolated sample is largely comprised of disk galaxies, even at the lowest masses.

2.3. HI Observations

We have obtained 317 HI observations with a signal-to-noise ratio (S/N) greater than 2 in an observing program spanning 2005 July to 2014 September; see G06 for an introduction to these data. After 2008, we focus our observations on isolated, low-mass, highly inclined (an axis ratio less than 0.65) galaxies from the NSA catalog described above with $d_{host} > 1.5$ Mpc, $M_* \leqslant 10^{9.5} M_\odot$.

All single-dish, unresolved HI measurements were obtained using the 305 m Arecibo Telescope (AO) and the 100 m Green Bank Telescope (GBT). For observations at AO in 2005 (hereafter AO2005), we observed with the L-band Wide receiver using 1024 resolution channels with a bandwidth of 12.5 MHz and a velocity resolution of $2.6 \, \mathrm{km \, s^{-1}}$. For observations at AO in Spring 2013, Spring 2014, and Fall 2014 (hereafter AO2013, AO2014a, and AO2014b), we observed using the L-band Wide receiver using 4096 resolution channels with a bandwidth of 12.5 MHz and a velocity resolution of $0.65 \, \mathrm{km \, s^{-1}}$. For observations at GBT in 2005, 2006, and 2008 (we group all observations together as GBT2008), we observed using the L-band receiver using 8192 channels with a bandwidth of 12.5 MHz and a velocity resolution of $0.32 \, \mathrm{km \, s^{-1}}$. In all cases, position switched ON/ OFF observing and ON/OFF noise-diode calibration was used.

Our target galaxies have an average Petrosian 90% light radius (r_{90}) of $\sim 20''$, significantly smaller than the GBT and AO beam sizes ($9'$ and $3.'5$, respectively), therefore flux attenuation and pointing offsets should not significantly affect our observations. We remove galaxies from our sample in the rare instances where the beam size is less than r_{90}. We detail each observing run in Table 2, including average integration times, the number of reduced spectra, the number of high S/N spectra, the number of non-detections, and the number of unstable spectral baselines. For 371 successfully reduced

spectra, we make 317 detections of galactic HI emission. We do not detect HI emission in 54 cases, most of which are non-isolated galaxies from GBT2008. We discuss our non-detections further in Section 2.7.

2.4. HI Data Reduction and Measurements

While there exist many methods for determining the HI properties of 21 cm emission lines, we implement a simple and consistent method optimized to minimize user intervention and maximize reproducibility of our measurements. We measure the shape and total emission of each single-dish HI observation without assuming a functional form for the 21 cm line. We also automate our entire procedure following a preliminary quality-control check. Automating our measurement procedure enables us to use a Monte Carlo (MC) method for estimating random errors in our HI parameters (see Section 2.5).

We first use our observing notes to identify 23 spectra with bad spectral baselines which can significantly affect our HI measurements. If the signal cannot be differentiated from a noisy baseline then we discard the observation and add the galaxy to a future observing queue. Next, we perform a linear baseline fit to each polarization mode outside of the region of each galaxy's HI emission at the SDSS systemic velocity. Since we generally target isolated galaxies, we do not find overlapping signals in our spectra. We subtract the baseline fits from each polarization mode and average the two polarization modes.

To achieve higher S/N and ensure reliable detections with our measurement algorithm, we determine an optimal smoothing length for each observing resolution that produces the most accurate HI parameters in our reduction pipeline. We test for optimal smoothing lengths by degrading synthetic Gaussian signals over a range of realistic widths, integrated fluxes, and S/N levels. We use Hanning windows to smooth spectra to a resolution of $5 \, \mathrm{km \, s^{-1}}$ for all of our observations.

For each spectrum, we identify the systemic velocity channel using the optical SDSS redshift velocity. If a spectrum does not have an S/N greater than 2 within $100 \, \mathrm{km \, s^{-1}}$ of the systemic velocity, we flag the observation as a non-detection. We discuss non-detections as well as the sensitivity of our observations in Section 2.7.

Next we identify the peak flux, f_{peak}, within a $500 \, \mathrm{km \, s^{-1}}$ spectral window around the systemic velocity. We expand outward from the peak flux velocity channel and set the boundaries of the emission to the first locations where the spectrum drops below zero flux. We locate these boundaries using a copy of the spectrum that has been smoothed by twice the Hanning window smoothing length. This extra smoothing eliminates any spurious noise features within the HI emission that may drop below zero and cut the emission profile artificially.

We measure the velocity width at $0.5f_{\mathrm{peak}}$, W_{50}, by measuring the distance in velocity space between the first and last spectral channels with flux above $0.5f_{\mathrm{peak}}$. To ensure we have measured the most accurate value of W_{50}, we interpolate between the neighboring spectral channels on either side of the channel closest to $0.5f_{\mathrm{peak}}$.

We measure W_{50} in order to directly compare with published ALFALFA results. However, since we have no reason to assume that W_{50} is the best probe of the maximum circular velocity of all disk galaxies, we also measure W_{20}, the velocity width at $0.2f_{\mathrm{peak}}$. While W_{20} is more sensitive to noise in the

wings of the HI profile (Koribalski et al. 2004), our high S/N isolated galaxies may offer us a deeper dynamical probe into the HI disks than W_{50} and W_{20}. We therefore focus on W_{20} in our analysis below. We note that W_{20} is typically $25 \, \mathrm{km \, s^{-1}}$ larger than W_{50} in our isolated sample, similar to Koribalski et al. (2004).

We compute the integrated flux density, S_{21}, by integrating the flux between the channels of the emission line profile boundaries. In order to remove excess flux due to noise in the wings of the profiles, we fit a second order polynomial to the minima on either side of the emission profile between $0.5f_{\mathrm{peak}}$ and where the flux goes to zero, similar to the algorithm of Springob et al. (2005). Using these fits, we remove spurious signal from the wings of the profile that tends to positively bias our flux measurements. We have tested this method by degrading high S/N spectra and then measuring the flux and HI profile widths as the S/N decreases. We found this method effective down to S/N of 2.

We calculate the rms of the noise of each spectrum, σ_{rms}, by identifying the largest signal- and RFI-free spectral chunks on either side of the HI emission profile with minimum window widths of $200 \, \mathrm{km \, s^{-1}}$. Two windows are selected on either side of the emission line, beginning $\pm W_{50}/2$ away from the profile edges and extending out to the maximum extent of the spectral range. Each window range is then optimized by shrinking the window until the mean flux is less than $0.5 \, \mathrm{mJy}$ or the minimum window width is achieved. The restriction on the mean flux ensures that we select a chunk of the spectrum where the baseline is stable and no significant emission is contaminating our noise measurement. We track the mean flux in the signal-free and RFI-free portion of the spectrum to monitor baseline stability. We eliminate RFI by masking any single channels with 6σ emission or greater. We calculate the rms as the rms of the two signal-free, RFI-free, and baseline stable spectral chunks.

If multiple observations exist for a galaxy at the same telescope and observing run, each rms-weighted spectrum is co-added together. For multiple observations of the same galaxy over different observing runs, we compute the error-weighted mean of each HI parameter measured with our reduction method. We tune and test our HI measurement method with the ALFALFA40 data in Section 2.6. We calculate an S/N measurement for all of our observations following the ALFALFA survey, adopted from Equation (2) of Haynes et al. (2011),

$$\mathrm{S/N} = \left(\frac{S_{21}}{W_{50}} \right) \frac{w_{\mathrm{smo}}^{1/2}}{\sigma_{\mathrm{rms}}}, \qquad (1)$$

with each variable as defined above and where $w_{\mathrm{smo}} = W_{50}/10$ $[\mathrm{km \, s^{-1}}]$. Hanning smoothing redistributes spectral noise and therefore increases the S/N of our spectra. This smoothing creates dependencies in each channel on neighboring channels. This dependence is accounted for in w_{smo}. Haynes et al. (2011) calculates w_{smo} as half of the number channels across the smoothed 50% HI line width. So w_{smo} represents the number of independent channels in each HI line.

2.5. HI Parameter Error Estimation

To estimate random errors in our HI parameter measurements, we apply a MC technique. For each MC iteration, we add a random noise realization to the fiducial observed signal

using our estimate of the rms noise in each spectrum and then re-measure the HI parameters over 1000 trials. The errors of each HI parameter estimate are the rms of the difference between each MC realization and the fiducial value of the parameter estimate.

We note that our method of error estimation does not consider baseline stability and its influence on the integrated flux density, which may be a source of significant uncertainty. It is for this reason that we have visually inspected and removed any spectra with obvious baseline instability. We have also made an effort to obtain multiple observations of the same galaxies to inspect any additional systematic error (see the last paragraph of Section 2.6).

2.6. Homogeneous HI Measurements of ALFALFA

In addition to our observations of isolated low-mass galaxies, we have re-measured all ALFALFA spectra overlapping with our NSA catalog (from the 40% data release of Haynes et al. 2011). The ALFALFA survey is a blind, single-dish, flux-limited HI survey. The ALFALFA40 data release covers $\sim$2800 deg^2 of the sky and provides a significant amount of overlap with the SDSS footprint. We match ALFALFA HI sources where the HI center is within 25$''$ of the optical center of our NSA catalog, given the pointing accuracy of the survey (Haynes et al. 2011). We use the ALFALFA data to compliment our isolated low-mass sample with both non-isolated galaxies and massive galaxies.

Re-measurements are preformed primarily to maintain a homogeneously measured data set and to apply our MC error calculation. We do not visually inspect or baseline fit the ALFALFA40 data; instead, we begin with the baseline-corrected spectra from ALFALFA and cut on their quality code of 1 to ensure reliable detections. We run these ALFALFA40 data through our HI parameter measurement steps described in Section 2.4, convolving a three-channel Hanning smoothing window with the downloaded ALFALFA40 spectra.

Figure 1 shows the difference between our re-measurements and the original ALFALFA40 measurements in units of the error of each HI parameter between the two data sets added in quadrature. In general, both our re-measurements of W_{50} and S_{21} agree extremely well with the ALFALFA40 measurements. As expected, we find that just under 5% of galaxies lie beyond the $\pm 2\sigma$ level (4098 HI observations in Figure 1 (169 outliers lie beyond the 2.0σ boundaries in either W_{50} or S_{21}). We remove galaxies beyond the 2σ window from our sample because their emission line boundaries are ambiguous and we require minimal scatter in our analysis below. We also discard any galaxy where the error on either W_{50} or M_{HI} is two times the measured value or more. We recover 96% of the complete ALFALFA40 data set with our re-measurements.

We note an asymmetry in the 2D distribution of differences in W_{50} and S_{21} in Figure 1 where we underestimate W_{50} and overestimate S_{21} relative to ALFALFA. The cause of this is due to a difference in measurement methods. Since we measure W_{50} at 50% the peak flux without accounting for noise or the shape of the HI profile, our value of W_{50} will always be larger than ALFALFA since they account for the shape of the HI profile when calculating such line widths. This will tend to decrease the value of the peak flux and therefore ALFALFA will always measure an equal or larger value of W_{50}. The spectral boundaries for the ALFALFA measurement are manually
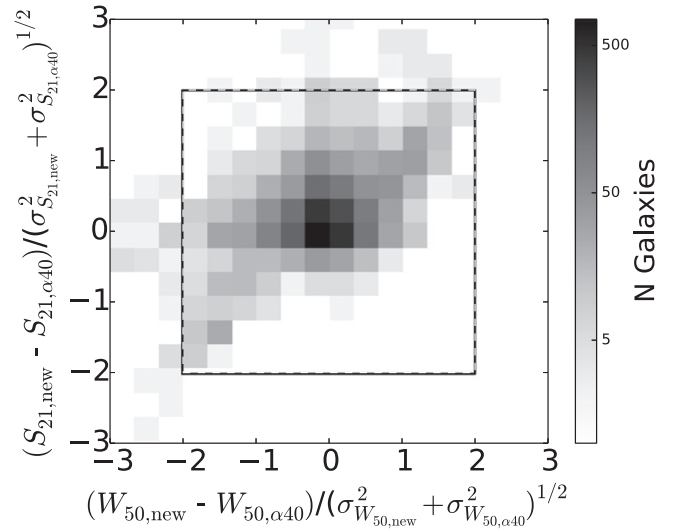

Figure 1. Two-dimensional distribution of the difference between our re-measurement of the ALFALFA spectra and the original ALFALFA measurement in units of σ, where σ is the error for each galaxy from the two data sets added in quadrature. The difference in 50% velocity width W_{50} and HI flux density S_{21} are plotted on the x- and y-axes, respectively. The number of galaxies in each bin are shown in the grayscale bar on the right. The overplotted box represents our selection boundaries ($\pm 2\sigma$) on the data. Any measurement outside of the box is discarded as a failed measurement. We discuss the asymmetry in the distribution at negative differences in W_{50} and positive differences in S_{21}, which is caused by a difference in measurement methods in Section 2.6.

marked by eye (see Haynes et al. 2011, Section 3 item 6). It is possible that this tends to remove some of the actual signal that overlaps with the noise features in the wings of the HI profile while our method of automatically marking spectral boundaries tends to include some fraction of the noise in the wings of our profiles. Since less than 1% of our measurements are beyond $\pm 1\sigma$ in this region, and 3% are beyond $\pm 0.5\sigma$, we proceed with our measurements. We also note that our analysis proceeds with W_{20}, which is less sensitive to noise in the peak flux and a more effective measurement of line width in the lowest mass galaxies. We will discuss this further in our future paper on the baryonic Tully–Fisher (BTF) relation.

Our HI observations overlap with 15 of the ALFALFA40 sample. We compare our HI parameter estimates to the original ALFALFA40 catalog for each overlapping galaxy. Most of our HI parameter estimates agree when compared to the original values from the ALFALFA40 data release. However, several measurements of S_{21} disagree between our GBT2008 observations and the original ALFALFA40 catalog. We assume that both our measurements and the ALFALFA40 measurements are correct and we attribute any differences to systematic errors that we have underestimated with our error estimation method (most likely due to baseline instability in the GBT2008 data). In order to bring our GBT2008 measurements into agreement with the ALFALFA catalog, we add 0.2 Jy km s^{-1} in quadrature to all of the GBT2008 S_{21} uncertainties. We present two pairs of overlapping galaxy spectra in Figure 2 for reference. In this figure, the top pair is a straightforward comparison while the bottom pair is more ambiguous.

2.7. Non-detections

Our observing strategy using the AO is to integrate until we measure a significant HI signal or until we reach a 25 minutes
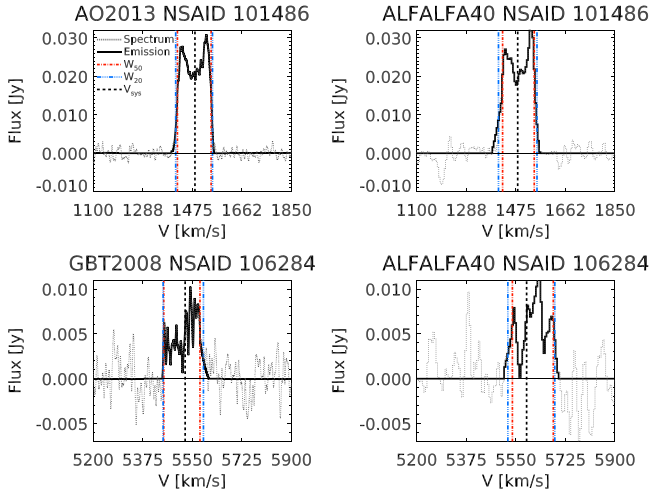
Figure 2. Sample pair of overlapping HI spectra between our sample and ALFALFA40. The left spectra are from our observations. The right spectra are from the ALFALFA40 data set. In all panels, the smoothed spectrum is plotted as a gray dotted line, the emission region is identified in solid black, the 50% and 20% flux boundaries are identified with red dashed–dotted and blue dashed–dotted–dotted vertical lines, respectively. The central velocity is marked with a vertical dotted black line. The top spectra are representative of a straightforward measurement, while the bottom spectra are more ambiguous due to the difference in spectral resolution. The more ambiguous cases will result in larger errors in W_{50} and S_{21} due to our method of estimating errors.

on-source integration time when possible. Most of our observations result in detection, but in some cases we do not detect significant HI emission. We define a non-detection as an observation with S/N < 2, the threshold where our measurement method begins to fail. Out of our 371 reduced spectra, 54 have an S/N less than 2. Nearly all of these low S/N observations are from GBT2008 since these observations were made before we implemented a fixed observing time criteria and focused our observations on isolated galaxies. Given the smaller dish size, the average GBT exposure leads to smaller S/N than an equivalent AO integration. Out of 144 isolated galaxies we observed using our post-2008 observing strategy, 7 are non-detections.

For all HI non-detections, we determine upper limits on S_{21}. First, we make preliminary estimates of atomic gas masses using the stellar-to-atomic gas mass relation in Section 3.2. Next, we estimate the inclination-corrected 50% velocity widths using the relation between baryonic mass and 50% inclination-corrected velocity widths, similar to the relation we describe in Section 3.3.1. We inclination de-correct this 50% velocity width to obtain an estimate of W_{50}. We initialize the value of S_{21} assuming a gas fraction of $f_{gas} = 0.98$.

Next, we create a synthetic Gaussian 21 cm emission line with an FWHM equal to W_{50} and a total integrated flux of S_{21}. We inject this initial Gaussian signal into 100 noise realizations using the measured σ_{rms} of our observation. After each noise realization, we reduce S_{21} by 10% and repeat a new set of noise realizations while we keep the FWHM of the Gaussian fixed. We repeat this procedure until the S/N drops below 2. The final injected values of S_{21} are reported as the upper limits of each non-detection. These upper limit estimates are plotted as light-colored, downward pointing arrows in all plots. Upper limits are excluded from our velocity–mass–size scaling relations and baryon fraction analysis since their velocity widths are contrived.

ALFALFA40 code 1 sources are all above the ALFALFA survey's S/N threshold of 6.5; therefore, upper limit calculations are unnecessary. Code 2 sources from ALFALFA40 have lower S/N and since they do not significantly impact our results below, we do not consider these data in our analysis.

2.8. Calculated and Inferred Quantities

We next describe the quantities derived directly from our HI line emission parameters and the optical parameters from the NSA catalog. In Table 1, we present a small sample of isolated low-mass galaxies from both our 255 original observations and the re-reduction of 4032 ALFALFA40 observations. Our complete data set is available upon request and will be publicly released once our HI observation program has concluded.

Distances (D) reported here are luminosity distances calculated from peculiar motion corrected redshifts (Willick et al. 1997). For our calculations and analysis, we assume that all of our galaxies are oblate, axisymmetric spheroids with symmetric mass distributions. We infer the observed inclination, $\sin i$, from the axis ratio as,

$$\sin i = \sqrt{\frac{1 - (b/a)^2}{1 - q_0^2}}, \qquad (2)$$

where q_0 is the intrinsic axis ratio, b/a is the observed axis ratio, and i is the inclination angle. Note that we limit the maximum value of the axis ratio b/a to 0.9995 to avoid dividing by zero in Equation (3).

The value of q_0 is traditionally fixed at about 0.2 at all stellar masses (e.g., G06; Begum et al. 2008). See Yuan & Zhu (2004) for a brief discussion on the history of q_0 as well as the distribution of q_0 as a function of morphology. The effect of q_0 on inclination corrections can be significant enough to change the slope and possibly affect the scatter of the BTF relation, (see Singhal 2008, Figure 1.8). We plan to discuss the effect of q_0 further in a future paper, where we will analyze circular velocities using the traditional value of $q_0 = 0.2$ as well as with a prescription for a changing q_0 as a function of stellar mass. In this work, we set $q_0 = 0.2$ throughout our analysis below.

We remove redshift broadening and we inclination correct the HI line widths to estimate a measure of maximum rotational velocity of the stars and HI gas disk in each galaxy as

$$V_{X,i} = \frac{W_X}{2 \sin i (1 + z)}, \qquad (3)$$

with $X = 50$ or $X = 20$ for either the 50% or 20% 21 cm line width, respectively. We perform these inclination corrections to W_X but we do not correct for non-circular motions (i.e., turbulence) which is typically assumed to be small (less than $20 \, km \, s^{-1}$). Note that in previous work, G06 corrected for non-circular motions. We note that the 20% velocity width has been shown by some authors to provide a better estimate of the true maximum circular velocity of the galactic disk (Verheijen 1997; Avila-Reese et al. 2008). We plan to discuss the effect of non-circular motions on HI velocity widths, as well as the accuracy of HI line widths as a probe of maximum circular velocity in a future paper. For now, we assume $V_{W20,i}$ is an accurate representation of maximum circular velocity.

We find that the inclination measurements for a small fraction of galaxies in our catalog fail due to the presence of central galactic bars. Inclination measurements fail when a face-on galaxy resembles the light distribution of a more edge-
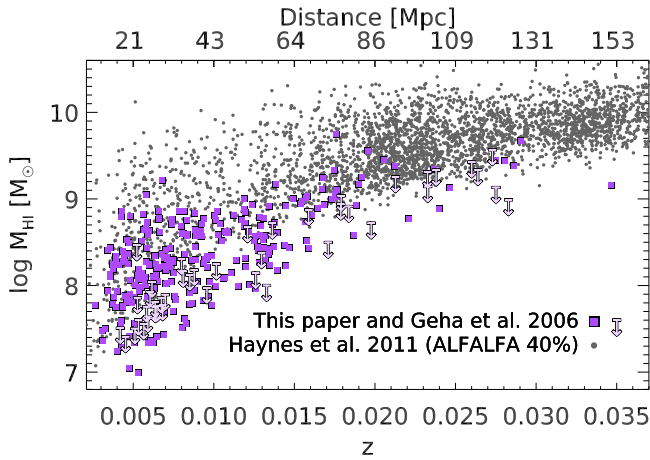
Figure 3. HI masses vs. peculiar motion corrected redshifts/distances of NASA Sloan Atlas galaxies that have been observed in 21 cm emission. Gray data points are our ALFALFA re-measurements. Purple squares are our own new and previously published (G06) observations with downward pointing, light-colored arrows representing upper limits on HI masses for non-detections. Our HI observations complement the ALFALFA survey at low masses and also overlap with the ALFALFA sample in several cases as a consistency check between data sets.

on galaxy due to the thin, centrally concentrated distribution of light of a galactic bar. We remove any barred galaxies that have been identified by the Galaxy Zoo project (Hoyle et al. 2011) from our analysis of circular velocities. We preserve these barred galaxies unless specified in our analysis below.

We calculate the HI mass from the S_{21} flux using the standard formula (e.g., Haynes & Giovanelli 1984) as

$$M_{HI} = 2.356 \times 10^5 \left(\frac{D}{\mathrm{Mpc}}\right)^2 \frac{S_{21}}{\mathrm{Jy\ km\ s^{-1}}} \left[M_\odot\right], \quad (4)$$

which assumes the HI gas disk is optically thin. We do not correct for HI self-absorption so our 21 cm flux measurements are lower limits due to the self-absorption of HI flux in a galaxy (Haynes & Giovanelli 1984; Haynes et al. 2011).

We present HI masses as a function of redshift in Figure 3. This figure shows the ALFALFA40 data set as gray points with our data and data from G06 plotted in purple. Our observations probe to lower HI masses at all redshifts than ALFALFA40.

We calculate atomic gas masses as $M_{gas} = 1.4 M_{HI}$ where the factor of 1.4 corrects for helium assuming solar abundances. We calculate "cold" baryonic masses as $M_{baryon} = M_{gas} + M_*$ with the atomic gas mass fraction defined as

$$f_{gas} = \frac{M_{gas}}{M_{baryon}}. \quad (5)$$

Note that our final cold baryon masses do not include dust, molecular gas, or ionized gas, the combination of which may contribute significantly to the baryon content of our galaxies (McGaugh & de Blok 1997; Cortese et al. 2012; Gnedin 2012). Further quantities, including stellar mass surface density and baryon fraction, are described in the appropriate sections below. We discuss the impact of molecular gas on our results in section Section 4.1.

2.9. HI Detection Limits, Isolated versus Non-isolated Sample Sizes, and Surface Brightness Limits

Here we discuss the relative sample sizes of our isolated and non-isolated galaxies as well as the surface brightness

limitations of the NSA catalog. We also discuss how a flux-limited HI survey affects our results and subsequent conclusions.

2.9.1. HI Detection Limits

The minimum HI mass detected by ALFALFA that overlaps with our catalog is $10^{7.2} M_\odot$, while the minimum HI mass detected by our observations is $10^{6.8} M_\odot$. Since the ALFALFA survey is flux-limited, it has not detected low-mass, HI-depleted galaxies such as satellites in dense groups and clusters (see Section 6 of Haynes et al. 2011 for a thorough discussion of the ALFALFA40 completeness). For the duration of this paper, we define detection limits as the minimum HI mass of either our data set or the ALFALFA40 catalog that overlaps with the NSA catalog.

When the ALFALFA survey is combined with our observations, the HI sample we study here is largely incomplete and biased toward blue, HI-rich, late-type galaxies (Haynes et al. 2011; Huang et al. 2012a).The median $g - r$ color for the ALFALFA survey and our HI data is 0.5 and 0.3, respectively. Satellite galaxies in the local group (Spekkens et al. 2014) and in the Virgo cluster (Cortese et al. 2011) are observed to be severely HI-depleted and would not be detected by either our observations or by ALFALFA. Therefore, even the relatively HI-depleted galaxies in our sample are still quite HI-rich compared to the average red sequence galaxy.

Due to our HI observation strategy, we have detected nearly every isolated galaxy identified optically. For the few isolated galaxies for which we have not made a detection, we calculate upper limits at relatively large atomic gas fractions. This is one of the primary results of our paper: all of the isolated galaxies that we have observed have either been measured at large atomic gas fractions or large atomic gas fractions cannot be ruled out via their upper limits (see Section 3.1). As for our comparison to non-isolated galaxies, our sample only glimpses into the HI-poor population that we expect to find in satellite galaxies. In our analysis below, we discuss these points further in context with our results.

2.9.2. Isolated versus Non-isolated Galaxy Sample Sizes

In order to disentangle internal galaxy evolutionary processes from the effects of environment, we select only the most isolated galaxies in the NSA catalog given our definition in Section 2.2. Although our overall HI sample is largely incomplete, we have made every effort to observe similar numbers of isolated and non-isolated galaxies at low stellar masses. Our analysis therefore assumes that the outliers we measure are significant and not simply an effect of the relative sample sizes between isolated and non-isolated galaxies.

For galaxies with stellar mass below $10^{9.0} M_\odot$, we have 429 non-isolated galaxies and 368 isolated galaxies with HI observations. We achieve an average fraction of isolated galaxies with HI observations of 0.46 for $M_* < 10^{9.0} M_\odot$, while the average fraction of isolated galaxies in the entire NSA catalog is 0.34. We assume that this relative sample size should allow us to rigorously compare the relations, distributions, and outliers as a function of environment.

2.9.3. Surface Brightness Limitations

Even though the NSA catalog has been optimized for nearby galaxies in the SDSS, the catalog still suffers from low surface

brightness completeness limitations. At a half-light surface brightness $\mu_{50,r} \sim 23.5$ mag arcsec^{-2}, the SDSS completeness drops below 50%. At $\mu_{50,r} \sim 24.0$ mag arcsec^{-2} the SDSS completeness drops below 10% (Blanton et al. 2005b, 2008; G12).

This surface brightness incompleteness impacts our study if either of two extreme situations exist: (1) we preferentially miss HI-poor galaxies, or (2) we preferentially miss gas-rich galaxies due to incompleteness.

If we preferentially miss HI-poor galaxies, then a HI-poor population of isolated galaxies might exist that has gone undetected. G12 compared the surface brightness distributions of low-mass, non-isolated galaxies to isolated galaxies via the two-sided K–S test and found that the two samples are likely drawn from the same distribution. Therefore, we have little evidence that suggests a larger number of HI-poor isolated galaxies at the low surface brightness end of the distribution are missing from our sample compared to the number of HI-poor, non-isolated galaxies.

The recent discovery of ultra diffuse galaxies (UDGs) in the Coma cluster by van Dokkum et al. (2015a, 2015b) using the Dragonfly Telephoto array (Abraham & van Dokkum 2014; Merritt et al. 2014) suggests that a significant population of galaxies with extremely low central surface brightness exists in galaxy clusters and the local field ($24 < \mu_{g,0} < 26$ mag arcsec^{-2}; Dalcanton et al. 1997). This may indicate that more low-mass galaxies (with $-13 < M_V < -17$) are missing from our SDSS sample than previously thought. It is possible that a similar population of UDGs exist in "the field." However, we have no evidence at this time that we are preferentially missing a *significant* number of isolated HI-poor UDGs.

We have no evidence that a significant number of HI-rich LSB galaxies are missing from our sample due to the following logic: we find that galaxies with surface brightnesses below $\mu_{r,50} < 23$ mag arcsec^{-2} have a median $f_{\rm gas}$ of 0.7 ± 0.2 (also see Schombert et al. 2001). Therefore, at all stellar masses where $\mu_{r,50} < 23$ mag arcsec^{-2}, galaxies should have atomic gas masses equal to or significantly greater than their stellar masses. These sources would be detected by ALFALFA but would have no optical counterparts in SDSS. The ALFALFA40 data release has found just ~ 50 extragalactic HI sources (out of 15,855) without optical counterparts in the SDSS DR7 and associated catalogs (Haynes et al. 2011; Cannon et al. 2015). This suggests that while such a population exists, these "dark galaxies" are rare.

3. RESULTS

We begin our analysis by inspecting the atomic gas fraction of galaxies as a function stellar mass and stellar mass surface density. We then compare the relation and scatter of stellar mass to atomic gas mass in isolated environments compared to non-isolated galaxies. We analyze the velocity–mass–size galaxy relations and the impact of environment on the slope, scatter, and correlation of these scaling relations. Finally, we investigate baryon fractions in these systems.

In Figures 4–7, we represent isolated galaxies with red squares and non-isolated galaxies with black dots. Whenever we exclude galaxies from our analysis, we preserve these data as gray points. We plot upper limits as light-colored, downward pointing arrows, color coded with environment. We also plot a hollow data point with a representative set of error bars

wherever error bars are not explicitly presented. In Figures 6 and 7, we plot non-isolated galaxies we determine to be gas-depleted as open blue dots. We have applied the Bayesian linear regression fitting method of Kelly (2007) for all linear fits below. This fitting method is particularly useful for linear models that also measure the intrinsic scatter of galaxy scaling relations.

3.1. Atomic Gas Fraction versus Stellar Mass

The fraction of baryons in atomic gas, $f_{\rm gas}$, is a strong indicator of the evolutionary state of a galaxy (e.g., McGaugh & de Blok 1997). Spheroidal, low-mass galaxies in dense environments can be almost completely depleted of HI gas, such as the satellite galaxies of the Local Group (e.g., Spekkens et al. 2014). Low-mass galaxies in moderately isolated environments have been shown to form stars slowly and in sparsely distributed regions (van Zee 2000, 2001) with star formation becoming more stochastic at low masses (Kauffmann 2014). In fact, the timescale for gas consumption due to star formation alone in gas-rich, irregular, low-mass galaxies is ~ 20 Gyr (van Zee 2001; Roychowdhury et al. 2014).

Given the timescale for gas depletion due to star formation in low-mass galaxies and the fact that isolated low-mass galaxies are all forming stars (G12), isolated galaxies should contain a significant amount of baryons in atomic gas. We might also expect gas-depleted, low-mass galaxies to be located in dense regions and to have undergone environmental processes, as opposed to have experienced purely internal processes that might deplete atomic gas. Therefore, examining the atomic gas fractions of galaxies in isolation compared to denser environments can provide us with insight into how feedback processes and environmental effects regulate the atomic gas supply of galaxies.

We present the relation between stellar mass and atomic gas fraction in the left panel of Figure 4 and the relation between stellar mass surface density and atomic gas fraction in the right panel of Figure 4.

In Figure 4 (left), at stellar masses above $\sim 10^{9.25} M_{\odot}$, galaxies follow a scattered relation with an upper ridgeline on $f_{\rm gas}$ at all stellar masses. At stellar masses below $10^{9.25} M_{\odot}$, the atomic gas fraction appears to saturate at $M_* \sim 10^{8.75}$ with $f_{\rm gas} \sim 95\%$. This implies that high-mass galaxies are either more efficient at converting their gas into stars or are more effective at preventing gas from cooling than galaxies at low masses. The scale dependency on $f_{\rm gas}$ at low masses is not introduced simply because of our dynamic range in this figure. This fact is made more apparent by Figure 5, where a break in the relation between stellar mass and atomic gas mass is clearly observed.

While the median atomic gas fractions for isolated and non-isolated, low-mass galaxies are similar (0.81 ± 0.13 for isolated galaxies and 0.82 ± 0.16 for non-isolated galaxies), isolated galaxies present slightly less scatter in $f_{\rm gas}$ at fixed stellar mass. Indeed, non-isolated galaxies with $M_* < 10^{9.25} M_{\odot}$ here and satellite galaxies from the literature (e.g., Galactic dSphs from Spekkens et al. 2014) can inhabit nearly the full range of $f_{\rm gas}$ (from 0.00 to 0.95) while we observe all isolated galaxies with $M_* < 10^{9.25} M_{\odot}$ to have $f_{\rm gas} > 0.3$.

We test that the lack of isolated galaxies with $f_{\rm gas} < 0.3$ is not simply due to a sampling effect. Over 10,000 trials, we
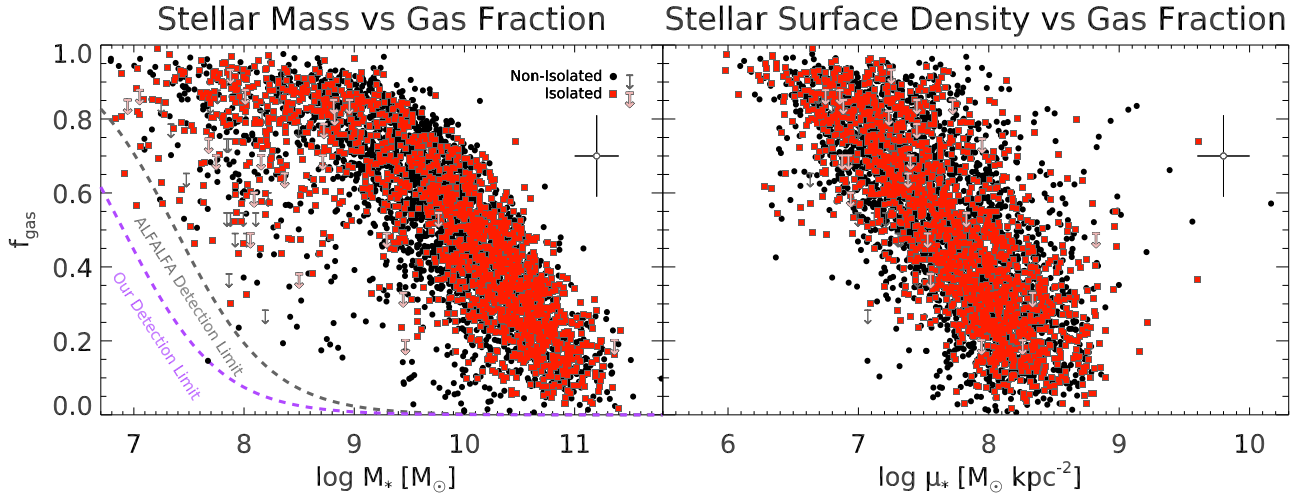
Figure 4. Left: atomic gas fraction vs. stellar mass. Black dots are galaxies that have not passed the isolation criteria described in Section 2.2. Red squares have passed the isolation criteria for each mass regime described in Section 2.2. We plot the median error bar for the entire sample as the open point, which is representative of the rest of the sample. This relation saturates at about $10^9 M_\odot$ in stellar mass. The dashed gray line represents the detection limit (minimum HI mass detected) of the overlap of our sample with the ALFALFA survey ($10^{7.2} M_\odot$). The dashed purple line represents the detection limit (minimum HI mass detected) of our HI observations ($10^{6.8} M_\odot$). Non-isolated galaxies are scattered to lower f_{gas} compared to isolated galaxies at nearly all stellar masses, indicating that environment affects the atomic gas fraction of non-isolated galaxies. Low-mass isolated galaxies are not found below an f_{gas} of 0.3. Right: atomic gas fraction vs. stellar mass surface density. We divide stellar mass by the square of the effective radius to show that stellar mass surface density is a better predictor of atomic gas fraction than stellar mass alone.
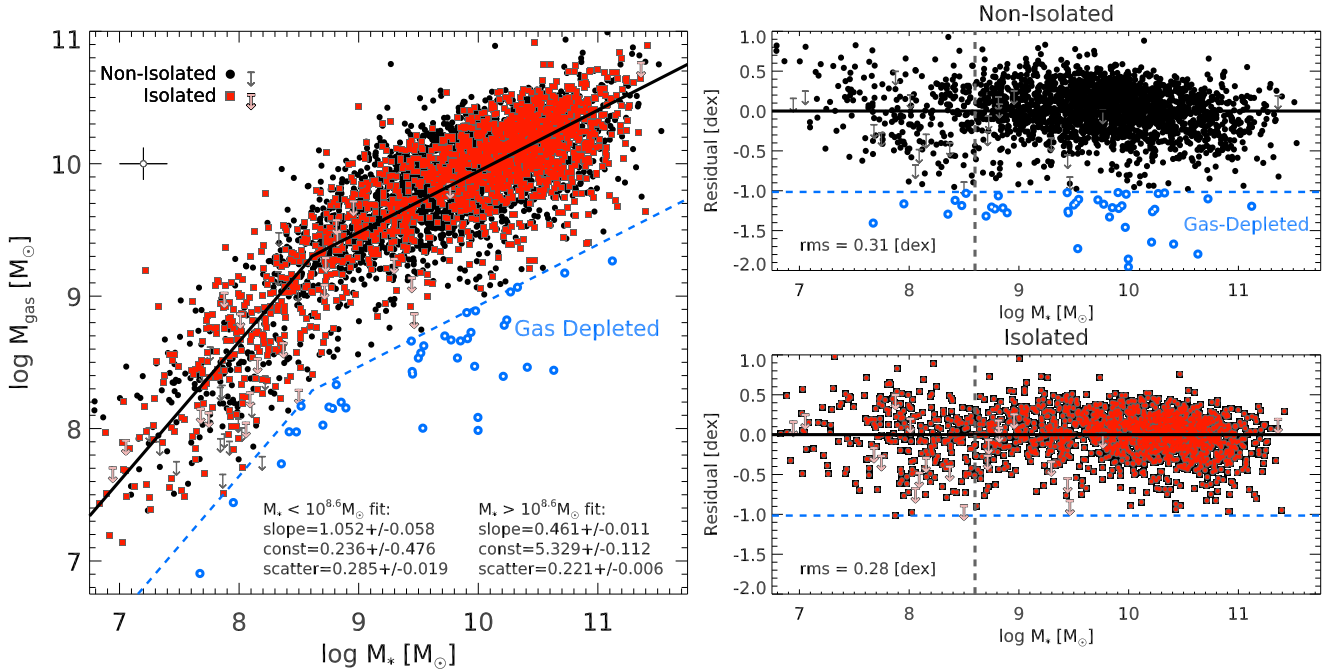
Figure 5. Left: atomic gas mass plotted as a function of stellar mass. Black dots are non-isolated galaxies and red squares are isolated galaxies. We plot the median error bar for the entire sample as an open point, which is representative of the rest of the sample. The fits here are listed below and in Table 3 and are plotted as the solid black line. We plot a dashed blue line representing the -1 dex threshold where we define galaxies to be gas-depleted when located below this threshold. We identify non-isolated, gas-depleted galaxies as open blue dots. Right: residuals to our fit as a function of stellar mass for all non-isolated galaxies (top right) and all isolated galaxies (bottom right). The break in the power-law is shown as a vertical, dashed gray line. The rms scatter of the residuals is listed at the bottom left corner of each panel. We plot a dashed blue line representing the -1 dex threshold where we define galaxies to be gas-depleted when located below this threshold. Note that no isolated galaxies are found below a residual of -1 dex. We plot non-isolated, gas-depleted galaxies as open blue dots. The non-isolated galaxies are slightly more scattered but the primary relation between stellar mass and atomic gas mass is the same for both the non-isolated and isolated galaxies.

randomly select the number of isolated low-mass galaxies ($N_{isolated} = 368$) with replacement from all 797 galaxies with $M_* < 10^{9.0} M_\odot$. On average, we draw five galaxies with $f_{gas} < 0.3$ and we always draw at least one galaxy with $f_{gas} < 0.3$. The complete lack of observed isolated galaxies with $f_{gas} < 0.3$ is therefore compelling evidence for the effects of environmental processes on atomic gas regulation.

We observe atomic gas fractions in our low-mass isolated sample that vary from 0.30 to 0.99. Therefore, isolated galaxies retain a significant fraction of baryons in atomic gas at low masses. The fact that we do not detect isolated low-mass galaxies with f_{gas} below 0.3 is a strong constraint on internal feedback processes, since it appears that feedback processes alone in low-mass galaxies does not remove all of a galaxy's

Table 3
Scaling Relations with $\log y = \alpha \log x + \beta \pm \epsilon$

Sample	x	y	α (Slope)	β (Constant)	ϵ (Scatter in log y)	Pearson r	Figures
Isolated only	$M_* < 10^{8.6}M_\odot$	M_{gas}	1.052 ± 0.058	0.236 ± 0.476	0.285 ± 0.019	N/A	5
Isolated only	$M_* \geqslant 10^{8.6}M_\odot$	M_{gas}	0.461 ± 0.011	5.329 ± 0.112	0.221 ± 0.006	N/A	5
Isolated only	M_{baryon}	r_{eff}	0.406 ± 0.007	-3.456 ± 0.074	0.159 ± 0.004	0.880	6
Non-isolated only	M_{baryon}	r_{eff}	0.390 ± 0.009	-3.293 ± 0.094	0.179 ± 0.004	0.764	N/A
All	M_{baryon}	r_{eff}	0.400 ± 0.006	-3.386 ± 0.059	0.171 ± 0.003	0.826	N/A
Isolated only	$V_{W20,i}$	r_{eff}	1.245 ± 0.033	-2.005 ± 0.069	0.209 ± 0.005	0.777	6
Non-isolated only	$V_{W20,i}$	r_{eff}	1.020 ± 0.039	-1.522 ± 0.083	0.225 ± 0.005	0.577	N/A
All	$V_{W20,i}$	r_{eff}	1.147 ± 0.026	-1.793 ± 0.054	0.219 ± 0.004	0.683	N/A
Isolated only	M_{baryon}	$V_{W20,i}$	0.277 ± 0.004	-0.672 ± 0.041	0.075 ± 0.002	0.916	6
Non-isolated only	M_{baryon}	$V_{W20,i}$	0.266 ± 0.005	-0.565 ± 0.050	0.080 ± 0.002	0.831	N/A
All	M_{baryon}	$V_{W20,i}$	0.272 ± 0.003	-0.624 ± 0.031	0.078 ± 0.002	0.878	N/A
Isolated only	$V_{W20,i}$	M_{baryon}	3.238 ± 0.046	3.210 ± 0.097	0.250 ± 0.008	0.916	N/A
Non-isolated only	$V_{W20,i}$	M_{baryon}	2.949 ± 0.053	3.834 ± 0.112	0.261 ± 0.007	0.831	N/A
All	$V_{W20,i}$	M_{baryon}	3.113 ± 0.035	3.482 ± 0.074	0.258 ± 0.006	0.878	N/A

Note. All linear relations fit in this paper. Sample, domain, range, slope, constant, scatter, Pearson r, and figure reference for each fit. For all mass–velocity–radius scaling relations, we have excluded galaxies with bars and with axis ratios greater than 0.65 from the galaxy scaling relation fits.

atomic gas. We note that the isolated galaxies with upper limit calculations cannot be conclusively ruled out as having lower atomic gas fractions than this limit. Feedback processes are most likely important in driving the large observed scatter in f_{gas} at low masses.

All but one non-isolated galaxy with $M_* < 10^9 M_\odot$ and $f_{gas} < 0.3$ are observed by the blind ALFALFA survey. For clarity, we have overplotted a dashed gray line in Figure 4 (left) that represents the smallest HI mass that overlaps with the NSA catalog and therefore the smallest f_{gas} that the ALFALFA survey could reach. Due to significantly longer exposure times, our observing program can detect galaxies at even lower atomic gas fractions than this gray line. We also overplot a dashed purple line in Figure 4 (left) that represents the smallest f_{gas} that our survey could have detected (the minimum HI mass detected by our observations is $10^{6.8} M_\odot$). We observe one non-isolated galaxy and two isolated galaxies below the ALFALFA limit. Also see Section 2.9 for a discussion of the sensitivity of our detections.

Galaxies with large f_{gas} are either less efficient at converting their gas into stars or these galaxies are accreting enough gas to replenish their star-making fuel supply. As expected from galaxies that follow the Kennicutt–Schmidt relation (see Zhang et al. 2009, Section 3.2) and from previous observations (e.g., Catinella et al. 2010; Cortese et al. 2011), we find that f_{gas} anti-correlates with the surface density distribution of stars. In the right panel of Figure 4, we present the relation between stellar mass surface density and atomic gas fraction. We calculate the stellar mass surface density as

$$\mu_* = \frac{M_*}{2\pi r_{eff}^2}, \qquad (6)$$

where r_{eff} is the effective radius which encloses 50% of the optical light. The effect of environment on f_{gas} is essentially removed from this relation, indicating that galaxies may evolve along this relation. The distribution of stellar mass density is clearly a better predictor of f_{gas} than stellar mass alone. The galaxies with the highest atomic gas fractions tend to have the lowest surface density of stars.

3.2. Gas Mass versus Stellar Mass

We present the stellar-to-atomic gas mass relation in the left panel of Figure 5. The slope of this relation steepens just below a stellar mass of $10^9 M_\odot$. This break in the relation is the cause of the saturation of f_{gas} at low mass in the left panel of Figure 4.

We fit a broken power-law to the high- and the low-mass isolated galaxies only. The fit breaks at $M_* = 10^{8.6} M_\odot$, where we find the two linear fits best intersect and minimize the scatter in the fits. This is a slightly lower stellar mass than our definition of a low-mass galaxy. We present our fits both in this panel and in Table 3. As discussed in Section 2.9, we find no evidence that this break in the power-law is due to a selection effect: we have no evidence that we have missed a significant galaxy population at low stellar mass and high atomic gas masses. This break in the power-law has also been observed by other studies (e.g., Huang et al. 2012a). The break in this relation implies that star formation is either much less efficient in low-mass galaxies or the HI gas in low-mass galaxies stays hot enough to prevent star formation but not hot enough to ionize the HI.

We inspect the residuals to our fits in the right panel of Figure 5. The residual panels demonstrate that scatter toward relatively small atomic gas masses is significant for non-isolated galaxies but not so for isolated galaxies. As discussed in Section 2.9, the non-isolated panel is certainly incomplete at low atomic gas fractions due to ALFALFA survey limits, yet we still observe many galaxies with relatively large negative residuals. In fact, we only detect non-isolated galaxies at residuals less than -1 dex. All isolated galaxies have either been either been detected in HI or cannot be ruled out at high HI masses via their upper limits. Therefore, we do not detect any isolated galaxies below a residual of -1 dex.

Note that -1 dex is more than -3σ away from our primary relation (see the rms values in each panel of Figure 5 (right)) and we plot a dashed blue line in both panels of this figure that represents residuals of -1 dex. Below this residual threshold, we define gas-depleted galaxies as open blue dots in this and our remaining figures for reference. We choose -1 dex as our residual threshold because we do not observe any galaxies above 1 dex in either sample and we do not observe any

isolated galaxies below -1 dex. These panels reinforce the idea that environmental effects preferentially remove atomic gas from non-isolated galaxies. The non-isolated outliers with residuals below -1 dex provide evidence that galaxies are depleted of atomic gas due to environmental processes.

3.3. Maximum Circular Velocity, Galaxy Mass, and Galaxy Size Relations

Distinct dark matter halos and their respective disk galaxy properties are related via galaxy scaling relations (e.g., Courteau et al. 2007; Avila-Reese et al. 2008). These relations are critical for studying models of galaxy formation and evolution (e.g., van den Bosch 2000; Dutton et al. 2007). We measure the velocity–mass–size scaling relations of our isolated disk galaxies using HI velocity widths, baryonic masses, and optical radii. Here we focus on galaxy scaling relations in isolation and compare our results to galaxies in denser environments.

In each panel of Figure 6, we present the velocity–mass–size relations as well as a fit to each relation using only unbarred, isolated galaxies with axis ratios less than 0.65. For comparison, we also plot the fit for non-isolated galaxies only as a yellow dashed line in each figure. As mentioned in Section 2.8, we have removed known barred galaxies from our analysis because their inclination measurements tend to fail. In Table 3, we present the results of fitting a linear model of $\log y = \alpha \log x + \beta \pm \epsilon$ to our data, where ϵ represents the intrinsic, random scatter in y. We also provide a measurement of the Pearson product-moment correlation coefficient (Pearson r) for each galaxy scaling relation. We provide model fits and Pearson r measurements for (1) all galaxies, (2) isolated galaxies, and (3) non-isolated galaxies.

We inspect the velocity–mass–size scaling relations of isolated disk galaxies. For maximum circular velocity measurements, we find that at $V_{W50,i} < 100$ km s^{-1} the inclination-corrected 50% velocity width can significantly deviate from the galaxy scaling relations of more massive galaxies; therefore, we use the inclination-corrected 20% velocity width ($V_{W20,i}$). For mass measurements, M_{baryon} has been shown to minimize the scatter of the BTF for low-mass, gas-dominated galaxies (McGaugh et al. 2000; McGaugh 2005, 2012; Stark et al. 2009). M_{baryon} should therefore provide the best mass measurement for studying galaxy scaling relations, as opposed to optical luminosity or stellar mass alone. Finally, we study the sizes of our sample using effective radii, r_{eff}. Other choices of Petrosian isophotal radii are similarly scattered.

3.3.1. Velocity versus Baryonic Mass

In Figure 6 (top left) we show the relation between baryonic mass and maximum circular velocity, the BTF. We present two slightly different fits to this relation in Table 3 using mass and velocity as the independent variable in each case. This relation is the most linearly correlated with a Pearson r of 0.916 and only slightly decreases to 0.831 for the non-isolated sample. The classical Tully–Fisher relation is between optical luminosity and circular velocity, while the BTF relates the total baryonic mass of the disk to the gravitational potential of the disk (Tully & Fisher 1977; Mo et al. 2010). When baryonic mass is used instead of luminous mass, galaxies at all masses follow a tight relation at all velocities (McGaugh et al. 2000). This indicates that despite being gas-dominated, low-mass,

irregular galaxies still follow the same fundamental relation as more massive, stellar-mass-dominated galaxies (McGaugh et al. 2009). Indeed, we observe a very small scatter of 0.075 for the isolated sample and 0.080 for the non-isolated sample. We do not observe a significant slope change due to environment. Gas-depleted, non-isolated galaxies are not preferentially scattered above or below this relation. We plan to examine the BTF relation in more detail in a future paper.

3.3.2. Radius versus Baryonic Mass

In Figure 6 (bottom left) we show the relation between radius and baryonic mass. The relation is linearly correlated with a Pearson r of 0.880 which decreases to 0.764 for non-isolated galaxies. This relation is an estimate of the overall density and thus the concentration of a galaxy. Firmani & Avila-Reese (2009) have shown that disk galaxies move along this relation as they evolve, indicating that we may not observe environmental effects on the baryonic mass to radius relation if radius and baryonic mass are both modified by environmental processes. Indeed, while non-isolated outliers exist, these outliers barely affect the fit, slope, and scatter of the relation. We note that gas-depleted, non-isolated galaxies are slightly scattered to either smaller radii or larger baryonic masses. Since these galaxies are actually deficient of baryons compared to galaxies of similar stellar mass, we assume that the radii of these gas-depleted galaxies are slightly smaller than the isolated sample.

3.3.3. Radius versus Velocity

In Figure 6 (bottom right) we show the relation between radius and maximum circular velocity. This relation is the least linearly correlated with a Pearson r of 0.777, which decreases to 0.577 for the non-isolated sample. The radius–velocity relation is related to the specific angular momentum of a galaxy. This relation is the most scattered of the three scaling relations. The scatter may be partially driven by the choice of radius, but relatively large scatter is predicted by models of galaxy formation (Avila-Reese et al. 2008). This relation presents the most significant slope change for a scaling relation due to environment, becoming shallower from 1.245 ± 0.033 for isolated galaxies to 1.020 ± 0.039 for non-isolated galaxies (also see Table 3 for a list of all fits). The scatter does not change when we fit on the isolated sample compared to the non-isolated sample. The change in slope implies that either the effective radius decreases for non-isolated galaxies at fixed circular velocity, or that circular velocities somehow increase. Non-isolated galaxies may be undergoing environmental effects that are changing the distribution of luminous mass and increasing the half-light radius of our systems. Gas-depleted, non-isolated galaxies tend to be slightly more scattered to smaller radii or higher maximum circular velocities. It is not obvious why the gas-depleted, non-isolated galaxies would be scattered to higher maximum circular velocities. Since we also observe a similar trend with radius as a function of baryonic mass, we assume that these gas-depleted galaxies tend to have slightly smaller effective radii than the isolated sample.

3.4. Baryon Fractions

If the atomic gas supply of galaxies is indeed dependent on environment, we would predict a higher measured baryon
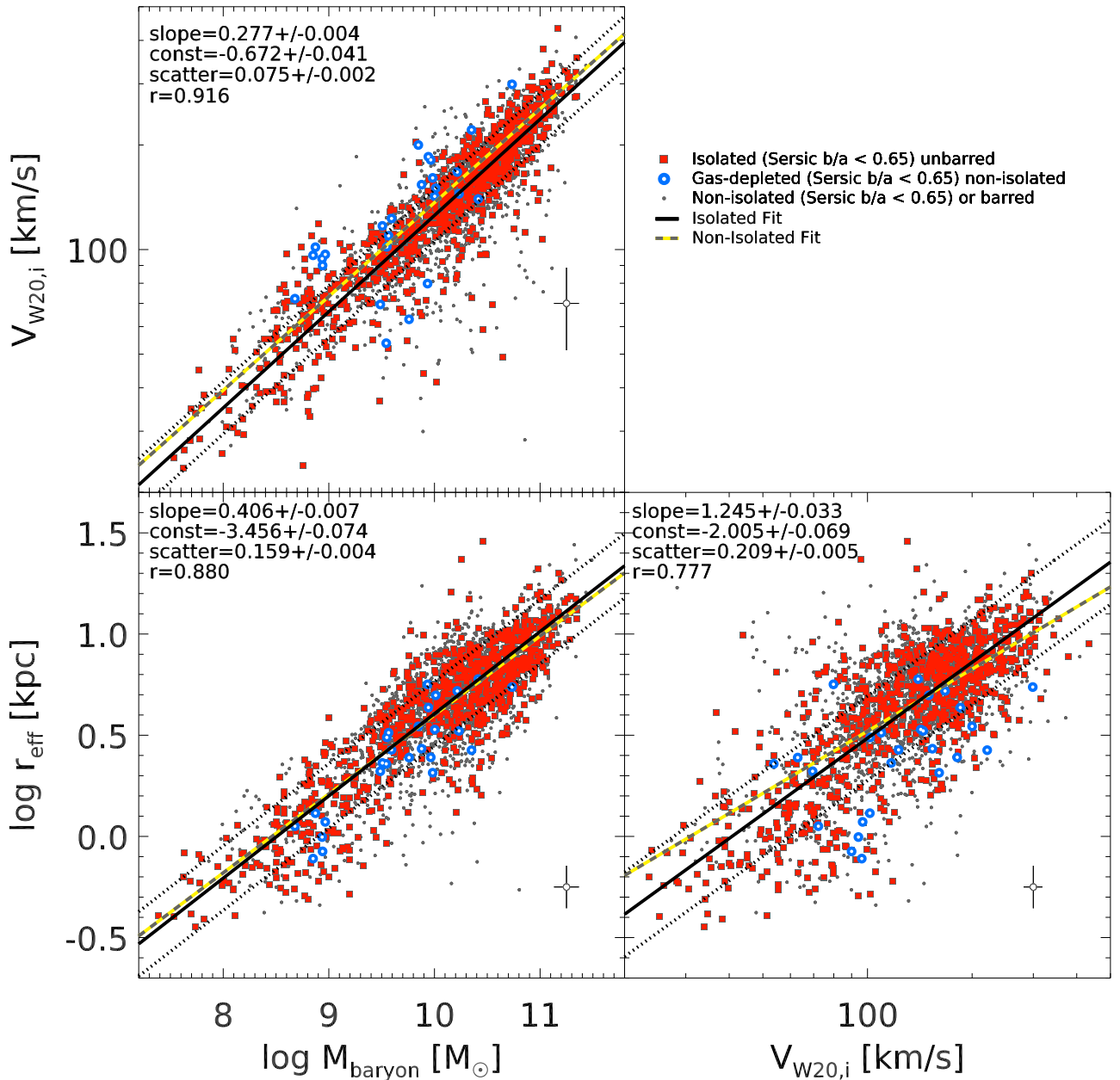
Figure 6. Velocity–mass–size scaling relations for $V_{W20,i}$, M_{baryon}, and r_{eff}. Unbarred, isolated galaxies with axis ratios less than 0.65 are plotted as red squares. Non-isolated galaxies with axis ratios less than 0.65 and barred isolated galaxies are plotted as gray dots for reference. Gas-depleted, non-isolated galaxies with axis ratios less than 0.65 are plotted as open blue dots. The slope, constant, scatter, and Pearson correlation rank (r) are listed in the top left corner of each panel. An open data point with representative error bars are plotted in the bottom right corner of each panel. The fit of each relation is plotted as a solid black line with $\pm 1\sigma$ scatter plotted as dotted black lines. We also plot the relations measured with the non-isolated sample only as dashed yellow lines for reference. The fits are similar for isolated, non-isolated, and both samples combined (see Table 3). The relation between $V_{W20,i}$ and r_{eff} appears to be affected by environment.

fraction in our isolated low-mass galaxy sample compared to galaxies that have had their atomic gas depleted by environmental processes. We define the baryon fraction of a galaxy as the total mass of baryons divided by the total mass of the galaxy (baryons plus dark matter).

The total baryonic mass of a galaxy is relatively straightforward to estimate. However, in calculating a galaxy's baryonic mass, we will always come up short of the actual baryonic mass due to missing contributions from dust, molecular gas, and ionized hydrogen. The total galaxy mass (baryons and dark matter) is much more ambiguous. The total galaxy mass can either be estimated as the total dynamical mass directly from the measured galaxy dynamics (hereafter the "disk baryon

fraction") or from indirect estimates of the total halo mass (hereafter the "halo baryon fraction"). In both cases, we define baryon fraction as:

$$f_{baryon,disk/halo} = \frac{M_{baryon}}{M_{dyn/halo}}. \tag{7}$$

In Figure 7, we present three different baryon fractions: one disk baryon fraction and two halo baryon fractions. For the calculations below, we assume that $V_{W20,i}$ is the maximum circular velocity of our galaxies.

The disk baryon fraction measures the fraction of baryons that have settled into the disk of the galaxy (i.e., the condensed
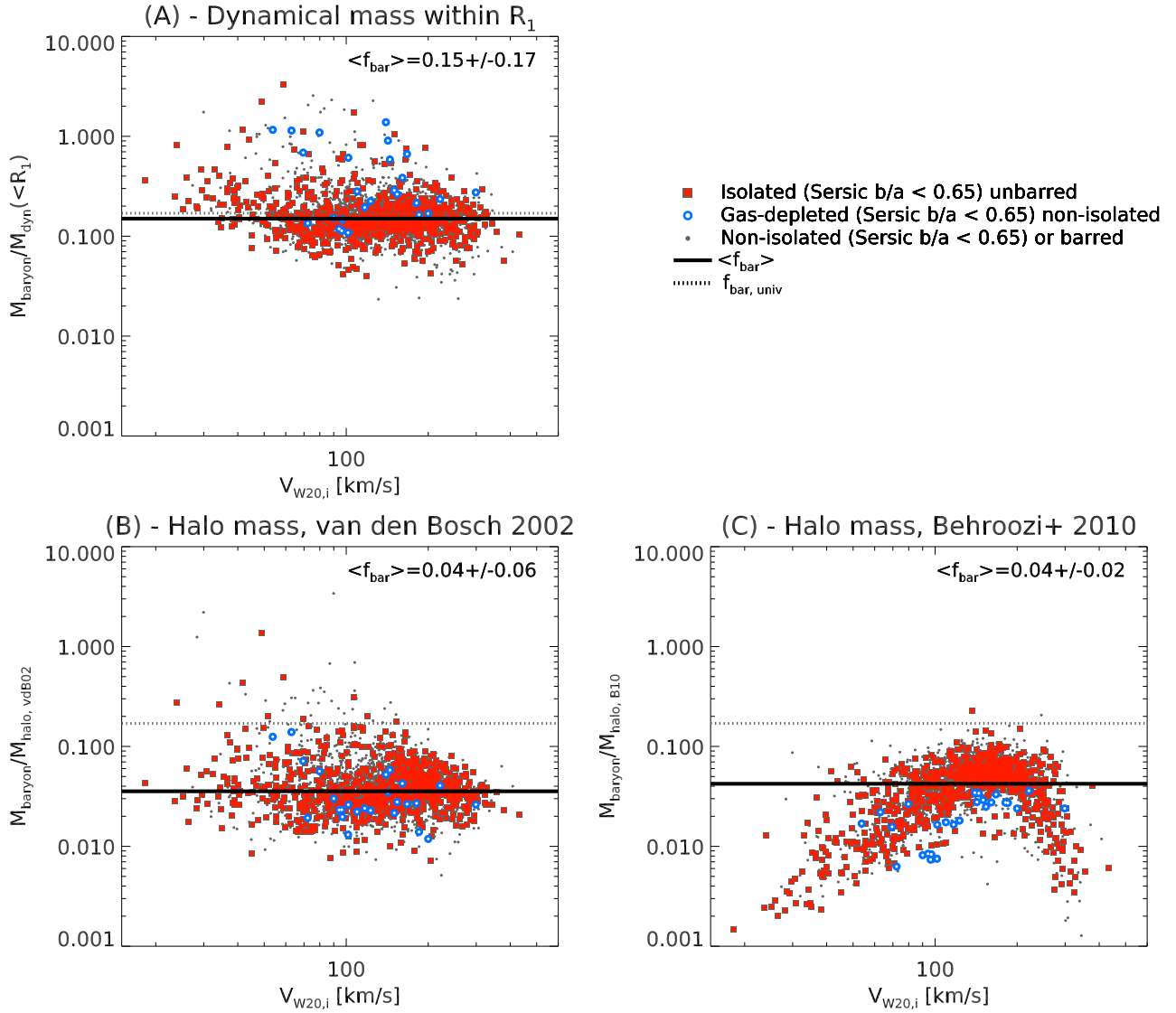
Figure 7. Disk (panel (A)) and halo (panels (B) and (C)) baryon fractions vs. circular velocity. Unbarred isolated galaxies with axis ratios less than 0.65 are plotted as red squares. Non-isolated galaxies with axis ratios less than 0.65 and barred isolated galaxies are plotted as gray dots for reference. Gas-depleted, non-isolated galaxies with axis ratios less than 0.65 are plotted as open blue dots. We plot the median baryon fraction as solid black horizontal lines. We plot the universal baryon fraction of 0.17 as a dotted horizontal line for reference. Typical uncertainties in $V_{W20,i}$ and $f_{baryon,disk/halo}$, given purely by error propagation, are on the order of 10 km s^{-1} and 0.01. We also output the median baryon fraction in the top right of each figure. The baryon fractions in panels (A) and (B) are calculated using the circular velocities we measure and result in flat relations. This is most likely due to the limitations of using HI circular velocities in low-mass galaxies where the HI gas may not probe out to V_{max}. The baryon fractions in panel (C) are measured independently of circular velocity, but it is the only panel where we find a strong relation with circular velocity.

baryon fraction of galaxies; Zaritsky et al. 2014). For disk baryon fractions, we assume that all of our galaxies are disk galaxies and that $V_{W20,i}$ has been measured at some radius related to the size of the HI disk. We calculate the total dynamical mass, which includes dark matter and baryons and assumes a spherical distribution of mass, as

$$M_{dyn}(<R_{HI}) = \frac{R_{HI} V_{W20,i}^2}{G} [M_\odot]. \qquad (8)$$

Since we do not have resolved HI rotation curves, we estimate the HI disk radius. We use the empirically derived relation of Broeils & Rhee (1997) between D_{HI} and M_{HI} (their Equation (3)), where D_{HI} is the HI disk diameter at a surface density of $1 M_\odot/pc^{-2}$,

$$\log M_{HI} = 1.96 \log D_{HI} + 6.52. \qquad (9)$$

This relation is calibrated with spiral and irregular HI-rich galaxies with $10^{7.9} < M_{HI} < 10^{10.3}$, (also see Hallenbeck et al. 2014; Wang et al. 2014). We define the HI disk radius as $R_{HI} = D_{HI}/2$.

de Blok & Walter (2014) have shown that 50% HI velocity widths originate at roughly $5R_D$, where R_D is the optical disk scale radius. The near equivalence of $5R_D$ and R_{HI} has been noted by de Blok & Walter (2014). We compare dynamical masses using these two estimates and find that R_{HI} and $5R_D$ produce similar results but R_{HI} results in a less scattered relation between circular velocity and baryon fraction.

We also compare dynamical mass estimates using R_{HI} to dynamical masses using the HI beam radius,

$$r_{\text{beam}} = D \sin\left(\frac{\theta_{\text{beam}}}{2}\right), \qquad (10)$$

where D is the distance to the galaxy and θ_{beam} is the angular size of the radio beam in 21 cm. The HI beam radius is the maximum radius at which we could have observed HI emission. Since we have not measured the actual radius of the disk's maximum circular velocity, this radius is the maximum radius that we could have possibly measured $V_{W20,i}$. Again, these radii give similar results, but the estimate using R_{HI} has the smallest amount of scatter in the relation below. Therefore, we chose to estimate only one disk baryon fraction. Note that if dark matter exists outside of the radius of the 21 cm observations (the beam), or if the rotation velocity profile is increasing beyond this radius and $V_{W20,i} < V_{\max}$, then we would estimate a larger baryon fraction.

We next calculate halo baryon fractions of our isolated galaxies using two different estimates of virialized halo mass. In their models, van den Bosch (2002 hereafter vdB02) find that the product of the square maximum circular velocity and the disk scale radius provide the best recovery of virial mass when compared to estimates using total galaxy luminosity or maximum circular velocity alone. We therefore calculate virial mass using scale radius and maximum circular velocity via Equation (15) of vdB02 as,

$$M_{\text{halo,vdB02}} = 2.54 \times 10^{10} M_\odot \left(\frac{R_D}{\text{kpc}}\right)\left(\frac{V_{W20,i}}{100 \text{ kms}}\right)^2. \qquad (11)$$

We assume exponential disks in our galaxies and set $R_D = 1.67 r_{\text{eff}}$. This is a valid approximation for most of our galaxies where the median Sérsic index is 1.3.

We also use the stellar mass to halo mass relation of Behroozi et al. (2010, hereafter B10). This relation between stellar mass and halo mass has been calibrated by taking advantage of the abundance matching technique. This technique assumes that stellar mass is directly related to halo mass with scatter less than 0.2 dex at all masses. For this halo mass estimate, B10 assume that the stellar mass function accurately maps onto halo mass function, even at the lowest masses where galaxies' baryonic masses are often dominated by atomic gas (Papastergis et al. 2012) and where many galaxies may be missed due to the surface brightness limitations of the input stellar mass function (Blanton et al. 2005b). B10 abundance match SDSS stellar mass functions to halo mass functions with virial masses at 337 times the mean background density at z = 0 (the same virial mass definition as vdB02). We use B10's Equation (21) with their free μ and κ model for $0 < z < 1$, and we call this mass estimate $M_{\text{halo,B10}}$.

In Figure 7, we present each of the three different estimates of baryon fractions. Uncertainties on $V_{W20,i}$ and f_{baryon} are typically on the order of 10 km s^{-1} and 0.01, respectively, given *purely* by error propagation. We list the median baryon fractions with rms scatter at the top right of each panel and as a yellow dashed horizontal line.

Panel (A) of Figure 7 presents a disk baryon fraction as a function of circular velocity. The next two panels ((B) and (C)) present halo baryon fractions as a function of circular velocity and stellar mass. For reference, we plot the universal baryon fraction $f_{\text{baryon}} = 0.17$ in each panel as a horizontal dotted line.

We discuss each panel of Figure 7. We visually inspect the SDSS images of outliers in each of the three panels.

A. We measure a median disk baryon fraction of 0.15 ± 0.17. This measurement is similar to the universal baryon fraction. We assume this is because we are measuring the dynamical mass at R_{HI} rather than the virial mass at R_{vir}, so we are not measuring a significant mass contribution from the dark matter halo. Galaxies at large baryon fractions are largely driven by mismeasured dynamical masses due to bars that have gone unidentified in Galaxy Zoo. These bars dramatically affect our baryon fractions due to the way we estimate dynamical masses using R_{HI} and $V_{W20,i}$. Galaxies at very low baryon fractions are mostly LSB galaxies. It also appears that the relation between HI mass and R_{HI} begins to break down at small circular velocities or that low-mass galaxies have larger baryon fractions in their galactic disks. Gas-depleted galaxies tend to lie at large baryon fractions, indicating that the dynamical masses can be severely underestimated when a galaxy is gas-depleted.

B. The halo baryon fraction estimate using the virialized halo mass of van den Bosch (2002), who fit the relation between $R_d V_{\max}^2$ and M_{vir}. The median value is 0.04 ± 0.06. Outliers at large baryon fractions are due to barred galaxies not identified by the Galaxy Zoo catalog, possible mergers, and irregular morphologies. Galaxies at very low baryon fractions are mostly LSB galaxies. Galaxies at small circular velocities do not show the upturn in baryon fraction that appears in panel (A); they remain constant at nearly all circular velocities, with significant scatter and a slight decrease in baryon fraction at high masses. Gas-depleted galaxies appear unperturbed from the primary relation.

C. The halo baryon fraction estimate using the stellar mass to halo mass abundance matching of Behroozi et al. (2010) recovers the only obvious relation between circular velocity and baryon fraction. While the dynamical masses estimated in panel (A) and the halo masses estimated in panel (B) are calculated using a power-law relation with maximum circular velocity, the B10 stellar mass to halo mass relation results in somewhat of an exponential relation with maximum circular velocity (not shown here). This relation flattens out at small circular velocities (below $\sim 70 \text{ km s}^{-1}$ and asymptotes at large circular velocities (above 200 km s^{-1}). For galaxies with $80 < V_{W20,i} < 100 \text{ km s}^{-1}$, the vdB02 and B10 baryon fractions are extremely similar because this is where the relations between maximum circular velocity and halo mass overlap. The B10 measurements of baryon fractions imply that both low-mass and high-mass galaxies are severely deficient of baryons compared to both the cosmic value. The median baryon fraction using this halo mass estimate is 0.04 ± 0.02, which is equal to, but less scattered than, the estimate in panel (B). Gas depletion in galaxies does not affect this estimate of halo mass, so gas-depleted galaxies simply lie at smaller baryon fractions than the rest of the sample.

In the cases above that estimate baryon fractions using halo mass, the measured baryon fraction is depleted compared to the universal baryon fraction. As we mentioned earlier, the baryon fractions of our galaxy sample must be somewhat depleted

since we have not detected all of the ionized gas, molecular gas, and dust in these galaxies. We assume that our atomic gas observations allow us to make reliable estimates of total baryonic mass. We discuss the impact of molecular gas on our results further in Section 4.1.

The scaling relation between maximum circular velocity and baryonic mass we measure in Section 3.3 suggests a weak correlation between maximum circular velocity and baryon fraction: We measure $M_{\mathrm{baryon}} \propto V^{3.238}$ and $r \propto V^{1/1.245}$ in Section 3.3. If we assume that $M_{\mathrm{dynamic}} \propto rV^2$, then $M_{\mathrm{baryon}}/M_{\mathrm{dyn}} \propto V^{0.435}$. We do not observe such a slope in the three panels above, i.e., this derived slope implies a smaller baryon fraction at low masses and a larger baryon fraction at high masses, but we observe a mostly constant baryon fraction in panels (A) and (B) above.

Since the precise value of r in our dynamical mass estimate is uncertain, we could instead assume a direct relation between total virialized mass and maximum circular velocity. We compare to the results of N-body simulations from Klypin et al. (2011), who find that $M_{\mathrm{vir}} \propto V_{\mathrm{max}}^{3.16}$ for distinct halos (see their Equation (8)). Given the previous paragraph, this would imply a roughly constant baryon fraction at all velocities, as in cases A and B above.

In general, we find that the baryon fraction is independent of environment. The lack of environmental dependence on baryon fraction is not surprising given our results in Section 3.3.1. We note that the scatter in baryon fraction doubles when the non-isolated galaxy sample is included. We find no evidence for severe baryon depletion in low-mass galaxies when we attempt to directly measure dynamical or halo mass, as opposed to the baryon deficiency using the abundance matching result. This result motivates further research into the most accurate measurement of halo mass in the lowest galaxy-mass regime.

4. DISCUSSION AND COMPARISON TO SIMILAR STUDIES

We discuss our results in context with similar studies, specifically in terms of environmental effects. We focus on results from the ALFALFA survey and other work that has inspected comparable HI observations of late-type galaxies at low redshift over similar galaxy-mass ranges.

4.1. Gas Fractions and the Gas to Stellar Mass Relation

Our relation between M_* and M_{HI} agrees well with Zhang et al. (2009), who use the homogeneous HyperLeda catalog and the SDSS DR4 to inspect the difference in HI masses for 800 metal-rich and metal-poor galaxies as a function of fixed stellar mass between $10^{7.5} M_\odot$ and $10^{11} M_\odot$. These authors find an offset between metal-poor and metal-rich galaxies, with metal-poor galaxies showing higher HI gas fractions than their metal-rich sample. These results suggest that galaxies with higher HI gas fractions are less evolved (at least chemically), indicating that our isolated low-mass sample at high atomic gas fractions are the least evolved galaxies at this mass scale. It may also be that these gas-rich galaxies have simply accreted a significant amount of low-metallicity gas.

The atomic gas content of SDSS DR7 galaxies has been studied extensively using the ALFALFA40 data set in Huang et al. (2012a, 2012b, hereafter H12a and H12b, respectively), as well as in Maddox et al. (2014). At low masses, H12a note a similar break in the relation of f_{gas} to M_* at $M_* = 10^9 M_\odot$. They

suggest this break is consistent with the effects of active galactic nucleus (AGN) feedback on the atomic gas content in massive galaxies. Recently, evidence of AGN has been found in galaxies with stellar masses as low as $10^{8.16} M_\odot$ (Reines et al. 2013), so the effect of AGN feedback must be less pronounced in low-mass galaxies for this to be true.

Why such a pronounced break in the stellar mass to atomic gas mass relation exists at this stellar mass is not entirely clear and is not predicted by existing models of galaxy formation (Maddox et al. 2014). Since the break in the relation is independent of environment, it is most likely due to internal processes of galaxy formation and star formation. Given the fact that we detect small fractions of baryons in these galaxies, we could assume that some significant component of baryons have gone undetected.

We estimate the amount of missing gas from high-mass galaxies using the low-mass end of the relation between stellar mass and atomic gas mass measured in Section 3.2. We find that high-mass galaxies would need roughly four times the measured HI mass in order to account for the break in the power-law. While it may be that high-mass, late-type galaxies contain a significant amount of molecular hydrogen (e.g., the Milky Way has roughly a three-to-one M_{HI} to $M_{\mathrm{H_2}}$ ratio (Draine 2011) and M94 has a one-to-one M_{HI} to $M_{\mathrm{H_2}}$ ratio; Leroy et al. 2009), the molecular gas mass in high-mass spiral galaxies appears at most to be comparable to the neutral atomic gas mass (McGaugh & de Blok 1997; Leroy et al. 2008; Saintonge et al. 2011). The amount of molecular hydrogen required to makeup this mass deficit would be extreme (e.g., Leroy et al. 2008), but combining this molecular gas with ionized gas may significantly reduce the discrepancy.

While the ionized gas content of galaxies is not well known, the molecular gas content of galaxies has been studied extensively (e.g., Kenney & Young 1989; Young & Scoville 1991; McGaugh & de Blok 1997; Welch et al. 2010). For instance, the AMIGA project has studied the M_{HI} to $M_{\mathrm{H_2}}$ ratio of isolated galaxies (see Figures 15 and 16 of Lisenfeld et al. 2011). Their results imply that galaxies must be strongly interacting in order to increase the ratio of molecular gas mass to neutral gas. This is most likely because the HI gas disk is less tightly bound than the molecular gas and is stripped first by environmental processes. We would not expect a significant number of such strongly interacting galaxies in our non-isolated sample due to the restriction that the HI beam is not confused between sources.

We estimate the molecular gas mass of our galaxies using Hα flux in the SDSS fiber to estimate the star formation rates (SFRs) for our galaxies. Since the SDSS fiber aperture is smaller than each galaxy, and would therefore underestimate global SFRs using the Hα flux directly, we correct for the missing Hα flux by computing the ratio of the r-band flux in a fiber aperture to the total r-band flux of the galaxy. To estimate molecular gas mass, we assume a relation between SFR and $M_{\mathrm{H_2}}$ (see Equation (1) of McGaugh & Schombert 2015). It may be that SFRs are affected by environment, so this exercise may reveal something about environmental effects on our galaxy sample (e.g., Perea et al. 1997).

We find the $M_{\mathrm{H_2}}$ to M_{HI} ratio of our sample lies between 0.04 and 0.08 and is highly scattered but fairly constant at all masses. We re-run our analysis and fitting algorithms and find that this estimate of molecular gas mass does not impact our results significantly. As expected, we have fewer gas-depleted,

non-isolated galaxies and the slopes of our relations change slightly. While the star formation efficiency of galaxies may not be significantly effected by environment (Casasola et al. 2004), the molecular gas fraction probably is. Therefore, an empirical estimate of molecular gas based on star formation efficiency arguments will not pick up on environmental effects if this was true. Also, we focus our work on low-mass galaxies and the molecular gas fractions of low-mass galaxies are observed to be much lower given their low surface brightness and lower HI surface densities (McGaugh 2012; Schruba et al. 2012). We plan to study the effect of environment on SFRs in a future work.

At high masses our data agree well with the GASS survey (Catinella et al. 2010), with their non-detections tracing much lower gas fractions than our sample. The GASS observing strategy is to observe until an atomic gas fraction threshold is reached. Their work can offer insight into non-isolated galaxy evolution at higher gas masses. We are focused on the low-mass regime so we forgo a detailed comparison to the GASS survey sample, but we note that GASS high-mass, non-isolated galaxies are gas-depleted relative to our gas-rich sample.

4.2. The Gas Content of Galaxies in Low-density Environments

H12a has shown that galaxies with $M_* > 10^9 M_\odot$ in the denser Virgo Cluster environment (Cortese et al. 2011) are gas-depleted compared to the primary gas-rich ALFALFA sample (see their Figure 2(c)). Cortese et al. (2011) claim that by comparing different models of Virgo dwarfs, they can determine that ram-pressure stripping is the cause of gas depletion in Virgo spirals as opposed to slow starvation. What is interesting about our results is that despite the ALFALFA40 sample being so gas-rich, we identify a small population of non-isolated galaxies that are noticeably gas-depleted compared to isolated galaxies. It would be interesting to compile a deep HI survey of non-isolated galaxies from the SDSS and probe this relation down to comparable atomic gas fractions as in Cortese et al. (2011).

While some effort has been made to study the HI content of void galaxies (e.g., Kreckel et al. 2012), our definition of isolated means not all isolated galaxies are located in voids and not all void galaxies are isolated. Therefore, results from studies of void galaxies may not be as useful as a direct comparison to our isolated galaxies. Regardless, Kreckel et al. (2012) find that low-mass void galaxies with stellar mass between $10^7 M_\odot$ and $10^9 M_\odot$ are *not* preferentially gas-rich. Our results suggest that depending on their definition, void galaxies may be still be affected by their local environment, especially at such low masses.

4.3. Scaling Relations

Our velocity–mass–size scaling relations agree well with similar studies of gas-rich spirals at higher masses (Courteau et al. 2007; Avila-Reese et al. 2008; Tollerud et al. 2010; Hall et al. 2012). Since we find that environment can affect the atomic gas fractions of galaxies, it would be logical that the scaling relations of these galaxies are also affected. While galaxy scaling relations become more scattered when non-isolated galaxies are included, we find that the galaxy scaling relations' slopes are not significantly perturbed compared to our isolated gas-rich sample.

It may not be that galaxies move perpendicular to scaling relations as they undergo environmental processes. Dutton & Bosch (2010) suggest that observed disk galaxies may evolve parallel to their scaling relations, which may be the case for galaxy evolution due to environmental processes.

For example, as a galaxy is stripped of atomic gas, it may not form stars at large radii where the binding energy is the lowest and the atomic gas is the most depleted. With its fuel reservoir depleted, a galaxy may also form fewer stars overall than a galaxy that has not been stripped of atomic gas. Therefore, as a galaxy decreases in radius due to environmental processes, it may also decrease in stellar mass, moving parallel to the scaling relation between effective radius and baryonic mass. In summary, the effect of environment on galaxies may be difficult to measure using the velocity–mass–size scaling relations.

It may also be that we do not observe a significant environmental dependence in galaxy scaling relations because the ALFALFA survey does not measure the scaling relations of gas-deficient disk galaxies due to the nature of a flux-limited survey. In the densest environments, such as in rich group environments (Catinella et al. 2013) and dense cluster environments (Kenney & Young 1989), the HI deficiency of galaxies increases dramatically as a function of radius from the X-ray center of the cluster (Boselli & Gavazzi 2006). Fernández Lorenzo et al. (2013) find evidence that massive isolated spiral galaxies with $10^{10} < M_* < 10^{11} M_\odot$ are larger than galaxies in denser environments at fixed mass.

When S0 galaxies are compared to the Tully–Fisher relation of spirals, an offset and an increase in scatter are observed (Neistein et al. 1999; Hinz et al. 2003; Bedregal et al. 2006; Williams et al. 2010; Davis et al. 2011). It has also been suggested that when galaxies are either disturbed, compact, or merging they do not follow the Tully–Fisher relation and the circular velocity must be added to the non-circular motions of the HI gas (Weiner et al. 2006; Kassin et al. 2007, 2014). Taking into account the velocity dispersion and concentration of a galaxy, disk and spheroidal galaxies follow similar scaling relations (Catinella et al. 2012). If spheroidal galaxies are transformed by their environment, then galaxies in groups and clusters should systematically vary from the scaling relations presented in this work. Indeed, Cortés et al. (2008) claim that environmental effects have decreased HI line widths in Virgo cluster galaxies. However, the most noticeable environmental effect on the galaxy scaling relations is that gas-depleted, non-isolated galaxies tend to be scattered to smaller effective radii than isolated galaxies—indicating again that we are not sensitive to environmental effects on circular velocity or that $V_{W20,i}$ is also encapsulating non-circular motion.

4.4. Baryon Fractions

We find that baryon fraction is independent of circular velocity in all cases except $M_{halo,B10}$. The baryon fraction calculated using $M_{halo,B10}$ shows a significant dependence on circular velocity because this estimate is based on stellar-to-halo mass abundance matching. This result is similar to Papastergis et al. (2012), who perform abundance matching with total baryonic masses using ALFALFA40 HI masses. These authors find that the depletion of baryons at low halo masses is only mildly alleviated when total baryon mass is used in the abundance matching technique. It has been suggested that LSB galaxies may significantly change abundance

matching results by changing the stellar mass function that goes into matching the halo mass function (Ferrero et al. 2012).

Our other baryon fraction estimates are at odds with the abundance matching technique which suggest baryon fractions are dependent on circular velocity and are much more significantly depleted of baryons. The flat relations we measure between circular velocity and baryon fractions at low circular velocities suggests that our HI velocity width measurement is not probing deep into the dark matter halo of low-mass galaxies (Ferrero et al. 2012). This could be confirmed by resolved HI synthesis maps. If the HI rotation curves do not reach the maximum circular velocity of the dark matter halo (e.g., several examples are available from Swaters et al. 2009), our $V_{W20,i}$ measurement would underestimate halo mass. This effect would lead to a flattening of the relation.

Blanton et al. (2008) find a weak relation between baryon fraction as a function of luminosity at low masses. Zaritsky et al. (2014) estimate the disk baryon fraction for a similar sample of gas-rich galaxies using the mass estimate of Bullock et al. (2001) and find a baryon fraction of 0.07. McGaugh et al. (2009) calculate the fraction of detected baryons to range from 0.83 for clusters to 0.0003 for the lowest mass dwarf galaxies. Our results do not indicate such a significant depletion of baryons in isolated galaxies with stellar mass $10^7 < M_* < 10^9 M_\odot$, nor do we note a significant trend toward low baryon fractions except in the B10 abundance matching estimate.

5. SUMMARY

We present new measurements of HI gas masses for 148 isolated galaxies with stellar masses between 10^7 and $10^{9.5} M_\odot$. We apply the same isolation criterion to our low-mass sample as G12 and extend this isolation criteria to galaxies at higher masses. We re-measure the HI masses and velocity widths of galaxies observed with the ALFALFA survey in order to create a large, homogeneous data set. Our HI data set represents the largest of its kind with such a rigorously defined isolation criteria.

Using these data, we study the baryon content of galaxies in isolated environments, specifically at low masses. We inspect the relation between galaxy stellar mass and atomic gas mass in isolated environments versus the relation in non-isolated galaxies (i.e., denser environments). We also examine the relations between velocity, mass, and size. Finally, we determine the disk baryon fractions and two estimates of halo baryon fractions for our galaxies. Our primary results are as follows.

1. We either place all isolated low-mass galaxies with stellar masses between 10^7 and $10^{9.5} M_\odot$ at high atomic gas fractions or we cannot rule out high atomic gas fractions via upper limits. Isolated galaxies have a median atomic gas fraction $f_{gas} = 0.81 \pm 0.13$ and atomic gas fractions always greater than 0.3.
2. We use a largely flux-limited sample of non-isolated, low-mass galaxies to derive a similar median atomic gas fraction as isolated galaxies. We measure non-isolated atomic gas fractions as low as 0.15, which is limited by the HI-rich galaxies of the ALFALFA survey.
3. We observe a break in the relation between stellar mass and atomic gas mass at $10^{8.6} M_\odot$. Both isolated and non-isolated galaxies follow this relation.

4. Only non-isolated galaxies are depleted in atomic gas by more than -1 dex compared to the atomic gas mass predicted by the stellar mass to atomic gas mass relation.
5. Environment does not significantly affect the linear correlations between velocity, mass, and size. Gas-depleted, non-isolated galaxies tend to be scattered to smaller effective radii.
6. Isolated galaxies follow a steeper relation between velocity and radius than non-isolated galaxies.
7. The baryon fraction of isolated galaxies is independent of environment: we measure a median baryon to dynamical mass fraction of $f_{baryon,disk} = 0.15 \pm 0.17$ and median baryon to halo mass fractions of $f_{baryon,halo} = 0.04 \pm 0.06$ using the results of semi-analytic models and $f_{baryon,halo} = 0.04 \pm 0.02$ using abundance matching.

The above results improve our understanding of the baryon content of low-mass galaxies and offer us some insight into the effect of environment in this stellar mass regime. Extending our analysis to galaxies below our stellar mass limit of $10^7 M_\odot$ requires deeper spectroscopic surveys (e.g., DESI) and deeper all-sky HI surveys (e.g., SKA). The flat relation we measure between circular velocity and baryon fraction motivates resolved, follow-up HI synthesis maps of our low-mass galaxy sample in order to determine the true maximum circular velocity of our systems and the radius where we measure this velocity. We plan to study the spatial distribution and the kinematics of baryons in our sample using integral field unit observations.

REFERENCES

Abraham, R. G., & van Dokkum, P. G. 2014, PASP, 126, 55
Aihara, H., Allende Prieto, C., An, D., et al. 2011, ApJS, 193, 29
Argudo-Fernández, M., Verley, S., Bergond, G., et al. 2014, A&A, 564, A94
Avila-Reese, V., Zavala, J., Firmani, C., & Hernández-Toledo, H. M. 2008, AJ, 136, 1340
Barton, E. J., Arnold, J. A., Zentner, A. R., Bullock, J. S., & Wechsler, R. H. 2007, ApJ, 671, 1538
Bedregal, A. G., Aragon-Salamanca, A., & Merrifield, M. R. 2006, MNRAS, 373, 1125
Begum, A., Chengalur, J. N., Karachentsev, I. D., Sharina, M. E., & Kaisin, S. S. 2008, MNRAS, 386, 1667
Behroozi, P. S., Conroy, C., & Wechsler, R. H. 2010, ApJ, 717, 379
Blanton, M. R., Eisenstein, D., Hogg, D. W., Schlegel, D. J., & Brinkmann, J. 2005a, ApJ, 629, 143
Blanton, M. R., Geha, M., & West, A. A. 2008, PASP, 682, 861
Blanton, M. R., Kazin, E., Muna, D., Weaver, B. A., & Price-Whelan, A. 2011, AJ, 142, 31
Blanton, M. R., Lupton, R. H., Schlegel, D. J., et al. 2005b, ApJ, 631, 208
Blanton, M. R., & Roweis, S. 2007, AJ, 133, 734
Boselli, A., & Gavazzi, G. 2006, PASP, 118, 517
Broeils, A. H., & Rhee, M. H. 1997, A&A, 324, 877
Brooks, A. M., & Zolotov, A. 2014, ApJ, 786, 87
Brough, S., Croom, S., Sharp, R., et al. 2013, MNRAS, 435, 2903
Bullock, J. S., Kolatt, T. S., Sigad, Y., et al. 2001, MNRAS, 321, 559
Cannon, J. M., Martinkus, C. P., Leisman, L., et al. 2015, AJ, 149, 72
Casasola, V., Bettoni, D., & Galletta, G. 2004, A&A, 422, 941
Catinella, B., Kauffmann, G., Schiminovich, D., et al. 2012, MNRAS, 420, 1959
Catinella, B., Schiminovich, D., Cortese, L., et al. 2013, MNRAS, 436, 34
Catinella, B., Schiminovich, D., Kauffmann, G., et al. 2010, MNRAS, 403, 683
Chabrier, G. 2003, PASP, 115, 763
Conroy, C., Prada, F., Newman, J. A., et al. 2007, ApJ, 654, 153
Cortés, J. R., Kenney, J. D. P., & Hardy, E. 2008, ApJ, 683, 78
Cortese, L., Catinella, B., Boissier, S., Boselli, A., & Heinis, S. 2011, MNRAS, 415, 1797
Cortese, L., Ciesla, L., Boselli, A., et al. 2012, A&A, 540, A52
Courteau, S., Dutton, A. A., van den Bosch, F. C., et al. 2007, ApJ, 671, 203
Croton, D. J., Farrar, G. R., Norberg, P., et al. 2005, MNRAS, 356, 1155
Dalcanton, J. J., Spergel, D. N., Gunn, J. E., Schmidt, M., & Schneider, D. P. 1997, AJ, 114, 635
Davis, T. A., Bureau, M., Young, L. M., et al. 2011, MNRAS, 414, 968
de Blok, W. J. G., & Walter, F. 2014, AJ, 147, 96
Draine, B. T. (ed.) 2011, Physics of the Interstellar and Intergalactic Medium (Princeton, NJ: Princeton Univ. Press), 5
Dressler, A. 1980, ApJ, 236, 351
Dutton, A. A., Bosch, F. C., Faber, v. d., M., S., et al. 2010, MNRAS, 410, 1660
Dutton, A. A., van den Bosch, F. C., Dekel, A., & Courteau, S. 2007, ApJ, 654, 27
Fernández Lorenzo, M., Sulentic, J., Verdes-Montenegro, L., & Argudo-Fernández, M. 2013, MNRAS, 434, 325
Ferrero, I., Abadi, M. G., Navarro, J. F., Sales, L. V., & Gurovich, S. 2012, MNRAS, 425, 2817
Firmani, C., & Avila-Reese, V. 2009, MNRAS, 396, 1675
Gallazzi, A., Bell, E. F., Wolf, C., et al. 2008, ApJ, 690, 1883
Geha, M., Blanton, M. R., Masjedi, M., & West, A. A. 2006, PASP, 653, 240
Geha, M., Blanton, M. R., Yan, R., & Tinker, J. L. 2012, ApJ, 757, 85
Gnedin, N. Y. 2012, ApJ, 754, 113
Grcevich, J., & Putman, M. E. 2009, ApJ, 696, 385
Gunn, J. E., & Gott, J. R. I. 1972, ApJ, 176, 1
Hall, M., Courteau, S., Dutton, A. A., McDonald, M., & Zhu, Y. 2012, MNRAS, 425, 2741
Hallenbeck, G., Huang, S., Spekkens, K., et al. 2014, AJ, 148, 69
Haynes, M. P., & Giovanelli, R. 1984, AJ, 89, 758
Haynes, M. P., Giovanelli, R., Martin, A. M., et al. 2011, AJ, 142, 170
Hinz, J. L., Rieke, G. H., & Caldwell, N. 2003, AJ, 126, 2622
Hoyle, B., Masters, K. L., Nichol, R. C., et al. 2011, MNRAS, 415, 3627
Huang, S., Haynes, M. P., Giovanelli, R., & Brinchmann, J. 2012a, ApJ, 756, 113
Huang, S., Haynes, M. P., Giovanelli, R., et al. 2012b, AJ, 143, 133
Hunter, J. D. 2007, CSE, 9, 90
Jarrett, T. H., Chester, T., Cutri, R., et al. 2000, AJ, 119, 2498
Karachentsev, I. D., Makarov, D. I., Karachentseva, V. E., & Melnyk, O. V. 2011, AstBu, 66, 1

Karachentseva, V. E. 1973, SoSAO, 8, 3
Kassin, S. A., Brooks, A., Governato, F., Weiner, B. J., & Gardner, J. P. 2014, ApJ, 790, 89
Kassin, S. A., Weiner, B. J., Faber, S. M., et al. 2007, ApJ, 660, 35
Kauffmann, G. 2014, arXiv:1401.8091
Kauffmann, G., White, S. D. M., Heckman, T., et al. 2004, MNRAS, 353, 713
Kelly, B. C. 2007, ApJ, 665, 1489
Kenney, J. D. P., Geha, M., Jáchym, P., et al. 2013, ApJ, 780, 119
Kenney, J. D. P., & Young, J. S. 1989, ApJ, 344, 171
Kirby, E. N., Bullock, J. S., Boylan-Kolchin, M., Kaplinghat, M., & Cohen, J. G. 2014, MNRAS, 439, 1015
Klypin, A., Karachentsev, I., Makarov, D., & Nasonova, O. 2014, arXiv:1405.4523
Klypin, A. A., Trujillo-Gomez, S., & Primack, J. 2011, ApJ, 740, 102
Komatsu, E., Smith, K. M., Dunkley, J., et al. 2011, ApJS, 192, 18
Koribalski, B. S., Staveley-Smith, L., Kilborn, V. A., et al. 2004, AJ, 128, 16
Kravtsov, A. V., Gnedin, O. Y., & Klypin, A. A. 2004, ApJ, 609, 482
Kreckel, K., Platen, E., Aragón-Calvo, M. A., et al. 2012, AJ, 144, 16
Leroy, A. K., Walter, F., Brinks, E., et al. 2008, AJ, 136, 2782
Leroy, A. K., Walter, F., Bigiel, F., et al. 2009, AJ, 137, 4670
Lisenfeld, U., Espada, D., Verdes-Montenegro, L., et al. 2011, A&A, 534, A102
Maddox, N., Hess, K. M., Obreschkow, D., Jarvis, M. J., & Blyth, S. L. 2014, MNRAS, 447, 1610
Martin, D. C., Fanson, J., Schiminovich, D., et al. 2005, ApJL, 619, L1
McGaugh, S., Schombert, J., Bothun, G., & de Blok, E. 2000, ApJ, 533, 99
McGaugh, S. S. 2005, ApJ, 632, 859
McGaugh, S. S. 2012, AJ, 143, 40
McGaugh, S. S., & de Blok, W. J. G. 1997, ApJ, 481, 689
McGaugh, S. S., & Schombert, J. M. 2015, ApJ, 802, 18
McGaugh, S. S., Schombert, J. M., de Blok, W. J. G., & Zagursky, M. J. 2009, ApJL, 708, L14
McGaugh, S. S., & Wolf, J. 2010, ApJ, 722, 248
Merritt, A., van Dokkum, P., & Abraham, R. 2014, ApJL, 787, L37
Mo, H., van den Bosch, F., & White, S. (ed.) 2010, Galaxy Formation and Evolution (Cambridge: Cambridge Univ. Press), -1
Moore, B., Katz, N., Lake, G., Dressler, A., & Oemler, A. 1996, Natur, 379, 613
Muldrew, S. I., Croton, D. J., Skibba, R. A., et al. 2011, MNRAS, 419, 2670
Neistein, E., Maoz, D., Rix, H.-W., & Tonry, J. L. 1999, AJ, 117, 2666
Papastergis, E., Cattaneo, A., Huang, S., Giovanelli, R., & Haynes, M. P. 2012, ApJ, 759, 138
Papastergis, E., Giovanelli, R., Haynes, M. P., & Shankar, F. 2015, A&A, 574, A113
Peñarrubia, J., Navarro, J. F., & McConnachie, A. W. 2008, ApJ, 673, 226
Peng, Y.-j., Lilly, S. J., Kovač, K., et al. 2010, ApJ, 721, 193
Perea, J., del Olmo, A., Verdes-Montenegro, L., & Yun, M. S. 1997, ApJ, 490, 166
Reines, A. E., Greene, J. E., & Geha, M. 2013, ApJ, 775, 116
Roychowdhury, S., Chengalur, J. N., Kaisin, S. S., & Karachentsev, I. D. 2014, MNRAS, 445, 1392
Saintonge, A., Kauffmann, G., Kramer, C., et al. 2011, MNRAS, 415, 32
Schombert, J. M., McGaugh, S. S., & Eder, J. A. 2001, AJ, 121, 2420
Schruba, A., Leroy, A. K., Walter, F., et al. 2012, AJ, 143, 138
Singhal, A. 2008, Proquest Dissertations And Theses, Univ. Virginia
Spekkens, K., Urbancic, N., Mason, B. S., Willman, B., & Aguirre, J. E. 2014, ApJL, 795, L5
Springob, C. M., Haynes, M. P., Giovanelli, R., & Kent, B. R. 2005, ApJS, 160, 149
Stark, D. V., McGaugh, S. S., & Swaters, R. A. 2009, AJ, 138, 392
Stierwalt, S., Besla, G., Patton, D., et al. 2015, ApJ, 805, 2
Swaters, R. A., Sancisi, R., van Albada, T. S., & van der Hulst, J. M. 2009, A&A, 493, 871
Tal, T., Dekel, A., Oesch, P., et al. 2014, ApJ, 789, 164
Tinker, J., Wetzel, A., & Conroy, C. 2011, arXiv:1107.5046
Tollerud, E. J., Boylan-Kolchin, M., Barton, E. J., Bullock, J. S., & Trinh, C. Q. 2011, ApJ, 738, 102
Tollerud, E. J., Bullock, J. S., Graves, G. J., & Wolf, J. 2010, ApJ, 726, 108
Toomre, A., & Toomre, J. 1972, ApJ, 178, 623
Toribio, M. C., Solanes, J. M., Giovanelli, R., Haynes, M. P., & Masters, K. L. 2011, ApJ, 732, 92
Tully, R. B., & Fisher, J. R. 1977, A&A, 54, 661
van den Bosch, F. C. 2000, ApJ, 530, 177
van den Bosch, F. C. 2002, MNRAS, 332, 456

van Dokkum, P. G., Abraham, R., Merritt, A., et al. 2015a, ApJL, 798, L45
van Dokkum, P. G., Romanowsky, A. J., Abraham, R., et al. 2015b, ApJL, 804, L26
van Zee, L. 2000, AJ, 119, 2757
van Zee, L. 2001, AJ, 121, 2003
Verheijen, M. A. W. 1997, PhD thesis, Univ. Groningen
Wang, J., Fu, J., Aumer, M., et al. 2014, MNRAS, 441, 2159
Weiner, B. J., Willmer, C. N. A., Faber, S. M., et al. 2006, ApJ, 653, 1027
Welch, G. A., Sage, L. J., & Young, L. M. 2010, ApJ, 725, 100
Wetzel, A. R., Tinker, J. L., Conroy, C., & Bosch, F. C. v. d 2014, MNRAS, 439, 2687

Wheeler, C., Phillips, J. I., Cooper, M. C., Boylan-Kolchin, M., & Bullock, J. S. 2014, MNRAS, 442, 1396
Williams, M. J., Bureau, M., & Cappellari, M. 2010, MNRAS, 409, 1330
Willick, J. A., Courteau, S., Faber, S. M., et al. 1997, ApJS, 109, 333
Yan, R. 2011, AJ, 142, 153
Yan, R., & Blanton, M. R. 2012, ApJ, 747, 61
Young, J. S., & Scoville, N. Z. 1991, ARA&A, 29, 581
Yuan, Q.-r., & Zhu, C.-x. 2004, ChA&A, 28, 127
Zaritsky, D., Courtois, H., Muñoz-Mateos, J.-C., et al. 2014, AJ, 147, 134
Zhang, W., Li, C., Kauffmann, G., et al. 2009, MNRAS, 397, 1243
Zolotov, A., Brooks, A. M., Willman, B., et al. 2012, ApJ, 761, 71